Journal of Computational Physics **179,** 704–735 (2002)
doi:10.1006/jcph.2002.7084

The Front-Tracking ALE Method: Application to a Model of the Freezing of Cell Suspensions

M. Jaeger* and M. Carin†

**IUSTI, CNRS UMR 6595, Univesité de Provence, Polytech'Marseille, Département Mécanique Energétique, Technopôle de Château Gombert, 5, rue Enrico Fermi, 13453 Marseille Cedex 13, France; and*
†Université de Bretagne Sud, Centre de Recherche, BP 92116, 56321 Lorient, France
E-mail: Marc.Jaeger@polytech.univ-mrs.fr and muriel.carin@univ-ubs.fr

Received July 17, 2001; revised March 6, 2002

A new front-tracking method to compute discontinuous solutions on unstructured finite element meshes is presented. Using an arbitrary Lagrangian–Eulerian formulation, the mesh is continuously adapted by moving the nearest nodes to the interface. Thus, the solution is completely sharp at the interface and no smearing takes place. The dynamic node adjustment is confined to global nodes near the front, rendering remeshing unnecessary. The method has been applied to the osmotic motion of a two-dimensional cell arising from a concentration gradient generated by a moving solidification front. The engulfment of one cell by an advancing solidification front, which rejects the solutes in a binary salt solution, is then computed. The results indicate that the ice increases the solute gradient around the cell. Furthermore, the presence of the cell, which prevents diffusion of the solute, leads to large changes in the morphology of the ice front.

Key Words: finite element method; front-tracking method; mesh fitting; ALE; cryobiology; solute; osmosis; phase change.

1. INTRODUCTION

Numerical simulation of transport problems with moving interfaces is an active field. For problems with highly convoluted interface topology, the fixed-grid approach has gained considerable popularity. The most widely used methods are those that track the interfaces indirectly, such as volume-tracking [1–3], level set [4, 5], and phase field methods [6, 7]. Less well-known are methods which follow the interfaces via connected marker particles. These methods generally lead to a finite element discretization of the interface, e.g., boundary integral methods. First developed by Glimm *et al.* [8], the efficiency and versatility of such front-tracking methods have mostly been demonstrated by the work of Tryggvason and co-workers [9, 10].

0021-9991/02 $35.00

Fixed-grid models have in common a smoothing of the interfaces over some finite width, at a minimum equal to the grid cell size. The main drawback of this approach is twofold: very fine grids are required to obtain accurate results, and the error induced by the smoothing decreases only linearly with grid refinement. This point is discussed, for example, in [11] and remedies have started to appear [11, 12]. In [13], Barth and Sethian state that "an interface smoothing could be delicate for a certain class of problems," especially when "jump conditions across the boundary are critical to both the solution of partial differential equations on either side of the interface and to evaluating the speed of the interface." This is precisely the situation explored in the present study.

The most widely used alternatives to the Eulerian approach are the boundary integral method [14, 15], the arbitrary Lagrangian–Eulerian (ALE) approach [16–19], including fully Lagrangian formulations [20–22], and more recently the space-time finite element and finite volume methods [23–25]. In principle, the ALE formulation is attractive, as it offers the possibility of switching between Lagrangian and Eulerian descriptions within the same computational domain. In practice, however, strong velocity differences at the interfaces lead to highly distorted meshes and remeshing becomes inevitable. To overcome this problem, we present a new method where mesh motion is restricted to the immediate vicinity of the interfaces.

The method can be viewed as a front-tracking method on fixed unstructured finite element meshes which are fitted to the interface locally at each time step. In this way we avoid interface smoothing. Very few interface mesh-fitting algorithms have been developed, probably due to the required introduction of irregular cells. The interface mesh-fitting algorithm introduced by Glimm *et al.* [8] was based on node displacement along the vertical and horizontal grid lines of a structured rectangular finite element mesh. The deformed elements, induced by this node motion, were regularized by introducing triangular elements. Alternatively mesh fitting can be obtained by dividing those cells crossed by the interface into several irregular cells. This approach has been used by Sato and Richardson [26] and Mashayek and Ashgriz [27] for structured finite volume meshes and by Lock *et al.* [28] for fully unstructured triangular finite element meshes. However, in this case it is impossible to control the size of the resulting element and, consequently, elements that are too small may be generated. With this in mind, a node displacement strategy is more efficient overall. The resultant motion of the mesh can be handled within the ALE framework, which is flexible and uses algorithms which are easily implemented into existing finite element codes.

The development of the model under consideration here was motivated by a study that we have initiated in the biophysics field [29]. In this study, we are concerned with the response of biological cells submitted to an osmotic stress during freezing in a cryopreservation process. One moving interface is the cell membrane, whose speed is directly related to the discontinuity in solute concentration between the internal solution (cytoplasm) and the external solution. Thus, the accuracy of the computed concentration at the front is crucial. The system is generally composed of several cells, capable of moving in different directions. The cell membrane is a thin-material shell submitted to mechanical stresses in response to deformations. While the cell motions suggest a Eulerian approach, the mechanical aspect is straightforward only with a Lagrangian description of the membrane motion, as knowledge of the deformation history is required. Thus, the membrane must be tracked explicitly with a separate interfacial mesh that is moved in a Lagrangian way. Although initially developed for this specific problem, the method has greater generality and can be extended to a broad range of applications.

The paper is organized as follows. A description of the front-tracking ALE method (FTALE) is detailed in Section 2. The method is applied to the study of the osmotic response of cells in a salt solution during freezing and the model is outlined in Section 3. Validation and convergence of the model with respect to osmosis and solidification is reported in Section 4. Finally, an example of one cell being engulfed in the solid phase is presented.

2. THE FRONT-TRACKING ALE METHOD (FTALE)

2.1. FTALE Formulation

We start the analysis by considering the one-dimension model equation

$$\frac{\partial \varphi}{\partial t} = \Lambda(\varphi(x,t)) \tag{1}$$

in Ω where Λ is a given differential operator. The domain Ω is crossed by a moving interface, corresponding to a jump in the φ field. The situation is depicted in Fig. 1 for an interface traveling from left to right. The numerical approximation of the time derivative $\partial\varphi/\partial t$ at time $t + \Delta t$ for a node that encounters an interface at time $t + \alpha\Delta t$, with $0 < \alpha < 1$, is obtained as follows.

Let $x^I(t)$ designate the location of the interface at time t, and let the interface encounter the node located at point x at time $t + \alpha\Delta t$: $x^I(t + \alpha\Delta t) = x$. At time t, $\varphi^-(x^I(t), t)$ and $\varphi^+(x^I(t), t)$ are the left and right values of φ at the interface, repectively. Here, the notion of left and right values is related to the orientation of the unit normal vector **n** to the interface.

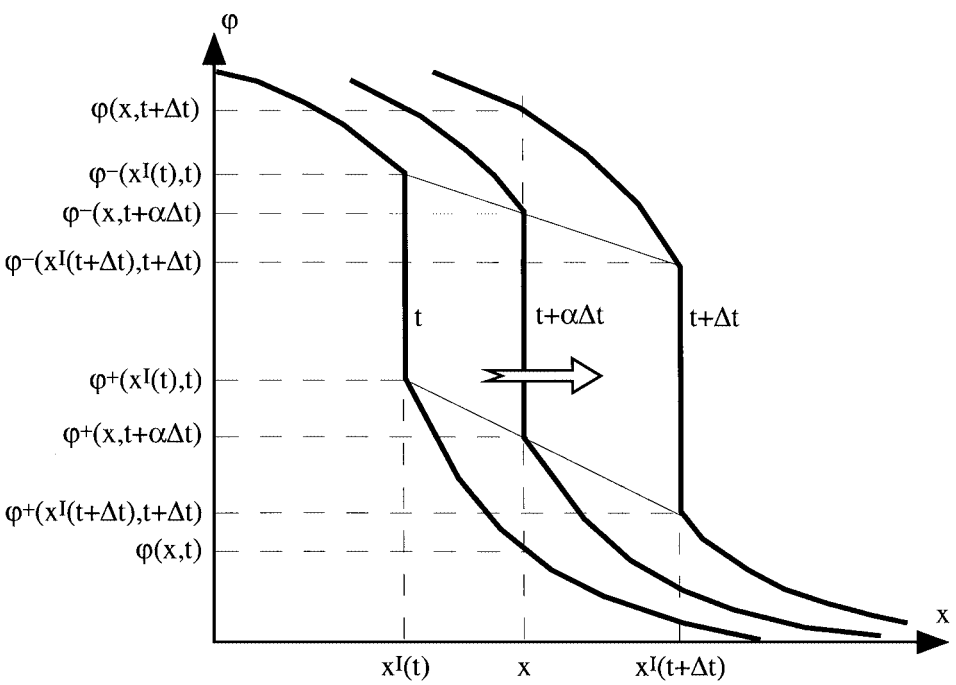

FIG. 1. One-dimensional representation of the jump of a scalar field φ near an interface traveling from left to right in the time interval $[t, t + \Delta t]$.

The time rate of change $\partial\varphi/\partial t$ at the interface can be approximated by

$$\left(\frac{\partial\varphi}{\partial t}\right)_{(x,t+\Delta t)} = \frac{\varphi(x,t+\Delta t)-\varphi^{-}(x,t+\alpha\Delta t)}{(1-\alpha)\Delta t}, \tag{2}$$

where $\varphi^{-}(x,t+\alpha\Delta t)$ can be estimated by the following interpolation expression:

$$\varphi^{-}(x,t+\alpha\Delta t) \approx \alpha\varphi^{-}(x^{I}(t+\Delta t),t+\Delta t)+(1-\alpha)\varphi^{-}(x^{I}(t),t). \tag{3}$$

For a first-order temporal discretization scheme, φ is approximated as

$$\begin{aligned}\varphi^{-}(x^{I}(t+\Delta t),t+\Delta t) &= \varphi^{-}(x+(1-\alpha)V\Delta t,t+\Delta t)\\ &\approx \varphi(x,t+\Delta t)+(1-\alpha)V\Delta t\left(\frac{\partial\varphi}{\partial x}\right)_{(x,t+\Delta t)},\end{aligned} \tag{4}$$

where V is the interface speed. Combining (2), (3), and (4) yields

$$\left(\frac{\partial\varphi}{\partial t}\right)_{(x,t+\Delta t)} \approx \frac{\varphi(x,t+\Delta t)-\varphi^{-}(x^{I}(t),t)}{\Delta t}-\alpha V\left(\frac{\partial\varphi}{\partial x}\right)_{(x,t+\Delta t)}, \tag{5}$$

which after some rearrangement results in an expression for the model problem

$$\left(\frac{\partial\varphi}{\partial t}\right)_{(x,t+\Delta t)} \approx \frac{\varphi(x,t+\Delta t)-\varphi^{-}(x^{I}(t),t)}{\Delta t}-\left(\frac{x-x^{I}(t)}{\Delta t}\right)\left(\frac{\partial\varphi}{\partial x}\right)_{(x,t+\Delta t)}. \tag{6}$$

The extension to the multidimensional case is straightforward,

$$\left(\frac{\partial\varphi}{\partial t}\right)_{(x,t+\Delta t)} \approx \frac{\varphi(\boldsymbol{x},t+\Delta t)-\varphi^{\pm}(\boldsymbol{x}^{I}(t),t)}{\Delta t}-\left(\frac{\boldsymbol{x}-\boldsymbol{x}^{I}(t)}{\Delta t}\right)\cdot(\operatorname{grad}\varphi)_{(x,t+\Delta t)}, \tag{7}$$

where $\varphi^{\pm}$ designates the left value φ^{-} or the right value φ^{+}, according to the direction of propagation of the interface. Here $\boldsymbol{x}^{I}(t)$ is considered to be the orthogonal projection of point $\boldsymbol{x}$ on the interface at time t.

From (7), the connection to an ALE formulation becomes obvious. Note that in this formulation, the node does not change sides, since it is treated as if it had been located on the interface at the previous time step. Viewed in this way, the node is dragged along by the interface up to its actual location. However, this mesh motion is used for illustrative purposes only; the deformed mesh enters into computation only through the addition of the extra advection term in (7).

The limiting case $\alpha = 1$ is of particular interest, as it represents the domain-mesh nodes located on the interface at time $t+\Delta t$. Most of these nodes belong to the set of nodes that has been moved onto the interface in order to fit the domain mesh. The ALE formulation (7) does not correspond to this mesh motion but instead considers these nodes as being swept along by the interface. Moreover, for these nodes right and left values of φ must be accounted for, in addition to the time derivative. Therefore, (7) is extended as follows:

$$\left(\frac{\partial\varphi}{\partial t}\right)^{\pm}_{(x=x^{I}(t+\Delta t)1+\Delta t)} \approx \frac{\varphi^{\pm}(\boldsymbol{x},t+\Delta t)-\varphi^{\pm}(\boldsymbol{x}^{I}(t),t)}{\Delta t}-\left(\frac{\boldsymbol{x}-\boldsymbol{x}^{I}(t)}{\Delta t}\right)\cdot(\operatorname{grad}\varphi)^{\pm}_{(x,t+\Delta t)}. \tag{8}$$

Here the subscript $\pm$ designates the right and left values of a quantity.

For a continuous field, a standard ALE formulation based on the real node motion, arising from the mesh fitting, is in principle adequate. However, in the case of a discontinuous normal derivative the standard formulation must be adjusted, and the FTALE provides an ideal mechanism. Finally, the true mesh motion is considered only for nodes that are moved back from the interface to their reference position after the interface has passed. This case is included in (7) as well.

The application of the FTALE method requires an interface mesh, a domain mesh, and a procedure for maintaining the interface properties. In the following subsections we describe the manner in which these components are implemented in two dimensions.

2.2. Interface Mesh

Each interface is represented by a finite element mesh, approximated by piecewise linear curves. This mesh is referred to as the "interface mesh" in contrast to the "domain mesh," used to solve the continuum mechanics problem.

In the time interval $[t, t + \Delta t]$, the motion of the node located at $\boldsymbol{x}(t)$ at time t is given by

$$\boldsymbol{x}(t + \Delta t) = \boldsymbol{x}(t) + \Delta t \boldsymbol{V}(\boldsymbol{x}(t), t), \tag{9}$$

where $\boldsymbol{V}(\boldsymbol{x}(t), t)$ is the interface velocity at time t and position $\boldsymbol{x}(t)$. The motion of the interface and thus its velocity $\boldsymbol{V}(\boldsymbol{x}(t), t)$ depends on the nature of the interface considered. In the case of a contact line separating two immiscible fluids, the velocity is simply given by that of the surrounding fluids. For a cell in a quiescent solution, the velocity of the membrane, neglecting the mechanical stresses, is proportional to the jump in solute concentration. For a solidification front, the jump in the thermal gradient determines the result.

The quality of the interface mesh is checked throughout the computation and nodes are added or deleted as needed. The refinement criterion is based on the size of the elements of the domain mesh (domain elements) surrounding the interfaces. We require that each element of the interface mesh (interface elements) be smaller than all its neighboring elements in the domain mesh. More precisely, the size of each interface elements is subject to the rule

$$\mathrm{LBH} < h_I / h_D < \mathrm{UBH}, \tag{10}$$

where h_I represents the size of an interface element and h_D that of its surrounding domain elements. LBH and UBH, the lower and upper bounds, respectively, are user-specified parameters.

2.3. Domain Mesh

The computational domain is discretized by fully unstructured triangular finite elements (T3). At each time step, a new mesh is built by fitting this "reference mesh" to the locations of the interfaces. The steps are as follows.

- A level set $\phi(\boldsymbol{x}, t)$, which corresponds to the signed distance to the nearest interface point, is constructed on the reference domain mesh. For each node of this mesh, the value of ϕ, the interface-mesh element containing the nearest interface point, and the location of this point in the element are stored as nodal properties.
- The elements of the reference domain mesh are classified into three groups according to the sign of ϕ.

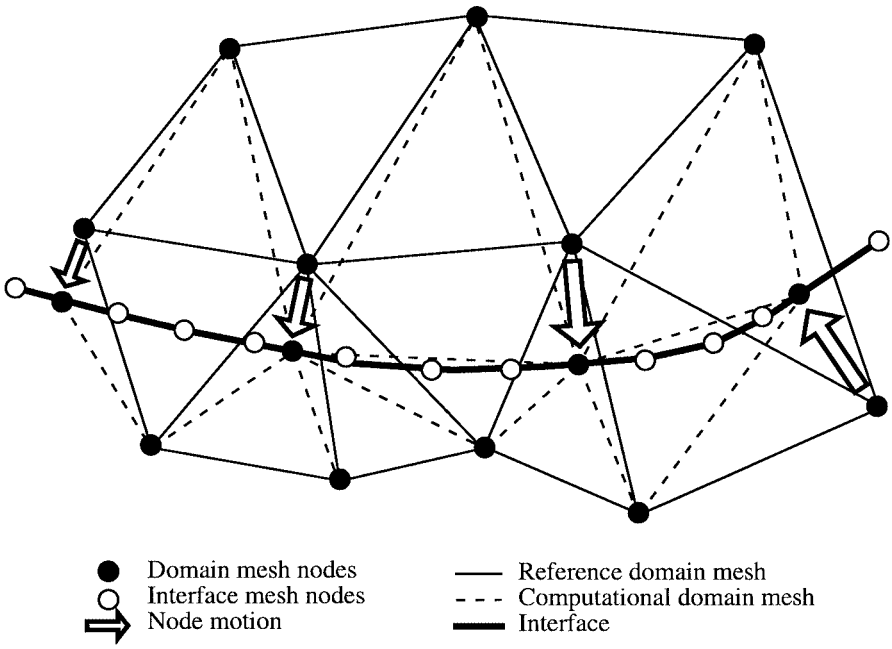

FIG. 2. Node motion involved in the mesh fitting.

(a) Group I: Element fully embedded in one medium ($\phi > 0$ (or $\phi < 0$) at all nodes of the element).

(b) Group II: Element embedded in one medium, but in contact with an interface at one or two of its three nodes ($\phi = 0$ at those nodes). Note that no element can have all its nodes located on an interface and that such an occurrence causes the simulation to abort.

(c) Group III: Element crossed by an interface (the sign of ϕ is not the same at the three nodes).

• Considering only the elements of the two last groups, the reference domain mesh is fitted to the interfaces by moving as many nodes as needed to their nearest interface points. The principle of this mesh fitting is sketched in Fig. 2. In this figure the domain mesh after adaptation (computational domain mesh) is represented by dotted lines. The set of nodes to be moved is not unique, and we select the configuration that best preserves mesh quality by comparing the Jacobians of the deformed elements. The value of ϕ for these nodes is set to zero and all material properties are updated. The data needed to give an accurate description of the interface, e.g., location, curvature, normal vector, and right and left values of the different physical fields, are stored as nodal properties of the interface-mesh nodes (white nodes in Fig. 2). These data are transferred to the nodes of the computational domain mesh, which are located on the interface using a straightforward linear interpolation.

Standard Lagrange-type triangular finite elements are used which ensure a piecewise linear approximation. To account for fields subject to jump conditions at the interface (e.g., solute concentration field), the previous mesh-fitting procedure is complemented by a special interfacial jump treatment in which the following steps are added.

• First, each node of the domain mesh (domain node) that is located on an interface is duplicated. The new node, hereafter referred to as the "twin node," is assigned to the elements

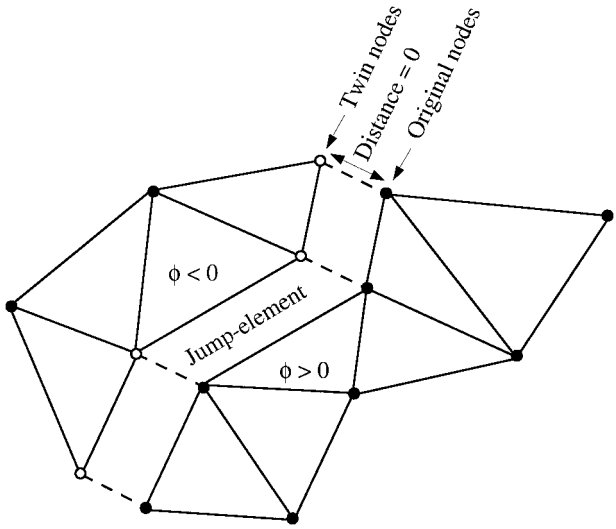

FIG. 3. Computational domain mesh in the interface region.

located on one side of the interface ($\phi > 0$) whereas the list of nodes of the elements located on the other side ($\phi < 0$) is unchanged. Therefore, the jump condition is the default mode; so, if continuity is desired, it must be enforced.

- Second, special boundary elements, "jump elements," are generated along each interface, connecting two subsequent couples of nodes (original twin). These can be viewed as degenerate quadrilateral four-node elements (Q4), which behave like two L2 boundary elements (see Fig. 3). The function of jump elements is to account for interfacial forces and fluxes, but they also enable communication between the elements located on each side of an interface.

3. FTALE MODEL TO STUDY THE FREEZING OF BIOLOGICAL CELLS

3.1. Physical Model

3.1.1. *Domain and Interface Definitions*

The physical system under consideration is a suspension of cells in a binary solution of salt. This system is cooled to below the freezing point, leading to the formation of an ice front which moves across the domain. Let Ω be the domain and $\partial\Omega$ its boundary. As depicted in Fig. 4, the domain contains three phases:

- a solid phase (ice) occupying the subdomain Ω_S with associated boundary $\partial\Omega_S$.
- an extracellular liquid phase (salt solution) occupying the subdomain Ω_L with associated boundary $\partial\Omega_L$.
- an intracellular phase (cytoplasm) occupying the subdomain Ω_C with associated boundary $\partial\Omega_C$; Ω_C can consist of multiple unconnected parts when there is more than one cell.

The interfaces separating these phases are of two different varieties:

- liquid–solid phase change front $\Gamma_{SL} = \partial\Omega_S \cap \partial\Omega_L$.
- cell membrane $\Gamma_{CL} = \partial\Omega_C \cap \partial\Omega_L = \partial\Omega_C$.

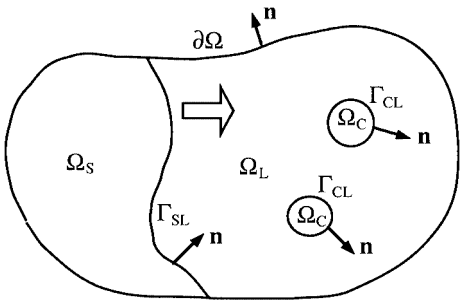

FIG. 4. Domain and associated boundary of each phase in the system (S = solid phase, L = liquid phase, C = cell).

3.1.2. *Equations of Heat Transfer and Solute Diffusion*

In the absence of fluid flow, which is not considered in the present study, the equations governing the heat and mass transfer are

$$\rho C_P \frac{\partial T}{\partial t} = \operatorname{div}(k \operatorname{grad} T), \tag{11}$$

$$\frac{\partial C}{\partial t} = \operatorname{div}(D \operatorname{grad} C), \tag{12}$$

where T is the temperature, ρ the density, C_P the specific heat, k the thermal conductivity, C the solute concentration, and D the solute diffusion coefficient. By design the model is able to deal with phase-dependent material properties which include the discontinuities at the interfaces. A jump in the density during liquid–solid phase change would imply a flow of the liquid phase. As this is not consistent with the no-flow assumption, the densities are set to be equal ($\rho^- = \rho^+ = \rho$).

3.1.3. *Membrane Interfacial Conditions*

The cell model used here is very simple. The membrane is modeled as an infinitely thin shell which can deform freely (mechanical stresses are not considered in this preliminary study) and is impermeable to the solute but not to water. Thus water flows in or out of the cell in the presence of a jump in the osmotic pressure. The interior ultrastructure of the cells has relatively little effect on the osmotic flow and the cells can be modeled as vesicles filled with a homogeneous medium. This last assumption is valid provided that the transport through the cytoplasm is much faster than through the plasma membrane.

The simplest mathematical description of the cell response to varying solute concentration in the ambient fluid is to assume that the fluid motion remains zero. For a single cell in a fluid with an initially uniform solute distribution, Batycky *et al.* [30] showed that fluid velocity is indeed zero while the cell changes volume due to osmotic flow of water through its boundary. Although this may not always be the case for nonuniform time-dependent concentrations, we assume here that it is valid. We also make the reasonable approximation that the partial volume of water is constant. Therefore, as water permeates the membrane, the membrane moves with equal and opposite velocity. The velocity of the membrane is then directly proportional to the difference in the solute concentration on the cell side of

the membrane, C^-, and on the fluid side, C^+, i.e.,

$$\boldsymbol{V}^{CL} = V^{CL}\boldsymbol{n} = -L(\Pi^+ - \Pi^-)\boldsymbol{n} \approx -LRT(C^+ - C^-)\boldsymbol{n}. \tag{13}$$

Here $\boldsymbol{n}$ defines the normal vector to the membrane directed toward the external medium, Π is the osmotic pressure, and R is the universal gas constant. L is the hydraulic permeability of the membrane and is temperature dependent according to the rule

$$L = L_{\text{ref}} \exp\left(\frac{-E}{R}\left(\frac{1}{T} - \frac{1}{T_{\text{ref}}}\right)\right), \tag{14}$$

where E is an activation energy and L_{ref} the value of the permeability at a given reference temperature T_{ref}. In a homogeneous external medium, (13) leads to the shrinking of cells for hypertonic environments ($V^{CL} < 0$) and to the swelling of cells in the hypotonic case ($V^{CL} > 0$).

Since the membrane is assumed to be impermeable to the solute, the influence of its motion on the concentration field can be modeled through a solute concentration flux, leading to the boundary condition

$$D^{\pm}(\text{grad}\, C)^{\pm} \cdot \boldsymbol{n} = D^{\pm}\left(\frac{\partial C}{\partial n}\right)^{\pm} = -C^{\pm}V^{CL}, \tag{15}$$

with $\boldsymbol{n}$ as previously defined.

The temperature is assumed continuous at the membrane, and the membrane interfacial condition for the heat transfer problem (11) is

$$T^{SL} = T^+ = T^-. \tag{16}$$

3.1.4. *Solidification Interfacial Conditions*

The velocity of the solidification front is given by the well-known Stefan condition, which expresses the energy balance along the solid/liquid interface

$$\rho^- \Delta H \boldsymbol{V}^{SL} = \rho^- \Delta H V^{SL}\boldsymbol{n} = \left(k^-\left(\frac{\partial T}{\partial n}\right)^- - k^+\left(\frac{\partial T}{\partial n}\right)^+\right)\boldsymbol{n}. \tag{17}$$

Here $\boldsymbol{n}$, the normal vector to the liquid–solid interface, is directed toward the liquid phase and ΔH is the latent heat of phase change.

The rejection of the solute at the moving ice front can be modeled in the same way as for the membrane, replacing V^{CL} with V^{SL} and C^- with zero in (15):

$$D^+(\text{grad}\, C)^+ \cdot \boldsymbol{n} = D^+\left(\frac{\partial C}{\partial n}\right)^+ = -C^+V^{SL} \quad \text{and} \quad D^-(\text{grad}\, C)^- \cdot \boldsymbol{n} = D^-\left(\frac{\partial C}{\partial n}\right)^- = 0. \tag{18}$$

The interfacial condition for the temperature is given by the Gibbs–Thomson relation

$$T^{SL} = T_m + mC^+ - \frac{\gamma T_m}{\rho \Delta H}\kappa - \frac{V^{SL}}{\mu}, \tag{19}$$

where T_m is the equilibrium melting temperature of the pure substance (water), m the slope of the linearized liquidus line from an equilibrium-phase diagram, γ the surface tension, κ the curvature of the interface, and μ the linear kinetic coefficient.

3.2. Numerical Model

The numerical model combines the FTALE approach and a 2D finite element method. The finite element formulation is obtained in the usual way and is described only briefly in order to focus on those aspects of particular interest to our model.

3.2.1. *Weak Formulation*

The ALE formulation of the evolution equations (11) and (12) are

$$\rho C_P \left(\frac{\partial T}{\partial t} - \boldsymbol{V}^{\text{FTALE}} \cdot \text{grad}\, T \right) = \text{div}(k\, \text{grad}\, T), \tag{20}$$

$$\frac{\partial C}{\partial t} - \boldsymbol{V}^{\text{FTALE}} \cdot \text{grad}\, C = \text{div}(D\, \text{grad}\, C). \tag{21}$$

Here $\boldsymbol{V}^{\text{FTALE}}$ is the velocity field associated with the fictitious mesh motion of the FTALE method, as described in Section 2.1. Recall from Eq. (7) that this velocity is $(\boldsymbol{x} - \boldsymbol{x}^I(t))/\Delta t$.

The heat equation (20) must be solved on the full domain Ω, including the solid phase Ω_S, the liquid phase Ω_L, and the cytoplasm Ω_C. The diffusion equation is solved in Ω_L and Ω_C, as it is zero elsewhere in Ω_S. The integral forms associated with the weak formulations of these two problems are

$$I_T = \int_\Omega \left\{ \rho C_P \delta T \left(\frac{\partial T}{\partial t} - \boldsymbol{V}^{\text{FTALE}} \cdot \text{grad}\, T \right) + k\, \text{grad}\, \delta T \cdot \text{grad}\, T \right\} ds$$
$$- \int_{\partial\Omega} k\, \delta T \frac{\partial T}{\partial n}\, dl - \int_{\Gamma_{SL}} \rho^- \Delta H \delta T V^{SL}\, dl, \tag{22}$$

$$I_C = \int_{\Omega_L \cup \Omega_C} \left\{ \delta C \left(\frac{\partial C}{\partial t} - \boldsymbol{V}^{\text{FTALE}} \cdot \text{grad}\, C \right) + D\, \text{grad}\, \delta C \cdot \text{grad}\, C \right\} ds - \int_{\partial\Omega_L \cap \partial\Omega} D\, \delta C \frac{\partial C}{\partial n}\, dl$$
$$- \int_{\Gamma_{SL}} \delta C C^+ V^{SL}\, dl - \int_{\Gamma_{CL}} \delta C^+ C^+ V^{CL}\, dl + \int_{\Gamma_{CL}} \delta C^- C^- V^{CL}\, dl, \tag{23}$$

where δT and δC are weighting functions.

In (22), the integral on Γ_{SL} cancels as the temperature at the solidification front is given by the Gibbs–Thomson condition (19). In (23), the contribution of the three integrals on Γ_{SL} and Γ_{CL} corresponds to the solute concentration fluxes induced by the motion of the interfaces, as given by (15) and (18). In both integral forms, the integrals associated with the boundaries $\partial\Omega$ are zero for Dirichlet or homogeneous Neumann conditions.

3.2.2. *Space Discretization*

We use Lagrangian triangular finite elements (T3) for the discretization of the domain integrals in (22) and (23). This yields continuous piecewise linear approximations for T and C and the associated weighting functions δT and δC. The interfacial jump conditions are accounted for by the duplication of the domain nodes located on the interfaces.

If needed, the discretization of the integrals on the boundary $\partial\Omega$ can be obtained by using two-node straight elements (L2) of Lagrange-type. Integrals on Γ_{CL} and Γ_{SL} are handled with the jump element introduced in Section 2.3, as contributions from each side of the interface must be considered.

3.2.3. *Time-Marching Scheme*

The first-order backward difference scheme is used for both the heat transfer and the solute diffusion problems. However, the model is not fully implicit since each problem is solved in turn, using the latest available data. The algorithm is as follows.

Interface updates:

- update of the interfaces locations.
- update of the topological properties of the interfaces via a cubic spline interpolation.
- update of the interfacial mesh.

Building the interface-fitted computational domain mesh:

- computation of the level set field ϕ.
- building the computational domain mesh.
- update of the material properties.
- transfer of data from the interfacial mesh to the computational domain mesh.

Solving the continuum mechanic problems:

- solving the solute diffusion problem.
- solving the heat transfer problem.
- transfer of data to the interfacial mesh.

3.2.4. *Determination of the Interfacial Speed*

By design the concentration jumps are accurately computed via FTALE without any additional treatment. The determination of the solidification front speed, however, needs additional consideration. Whereas (13) relates the interface velocity directly to the jump of the concentration field, the velocity of the phase-change front is related by the Stefan condition (17) to the jump of the normal derivative of the temperature. Lagrangian finite elements do not use derivatives as nodal degrees of freedom and moreover the first derivatives take constant values over each linear T3 element; thus the nodal values of the derivatives must be reconstructed. This is done by an averaging procedure which incurs some error, especially for triangular-shape elements and nonuniform meshes. For this reason, applying (17) turns out to cause instability.

Alternatively, the Stefan condition can be used in a weak form [31–34], which is very natural in a finite element framework. If δV^{SL} designates the weight function associated with the unknown velocity V^{SL}, the weak form of (17) is

$$\int_{\Gamma_{SL}} \rho^{-} \Delta H \delta V^{SL} V^{SL}\, dl = \int_{\Gamma_{SL}} \delta V^{SL} \left(k^{-} \left(\frac{\partial T}{\partial n} \right)^{-} - k^{+} \left(\frac{\partial T}{\partial n} \right)^{+} \right) dl. \qquad (24)$$

The right hand side of (24), related to the weak form of the heat transfer problem (22), can be obtained after the heat transfer problem has been solved. Indeed, one can select for the integral form (22) weight functions δT, which cancel everywhere except on the element with nodes located on Γ^{SL}. We designate these functions $\delta T|_{\Gamma SL}$. Their restrictions to Γ^{SL} constitute the set of weigh functions δV^{SL} considered in the weak formulation (24), when L2 elements are used to define the approximation of V^{SL}. These L2 elements can be seen as the trace on Γ^{SL} of the T3 element setting. Thus, the right hand side of (24) is given by

$$\begin{aligned}
&\int_{\Gamma_{SL}} \delta V^{SL} \left(k^- \left(\frac{\partial T}{\partial n} \right)^- - k^+ \left(\frac{\partial T}{\partial n} \right)^+ \right) dl \\
&\quad = \int_\Omega \left\{ \rho C_P \delta T|_{\Gamma_{SL}} \left(\frac{\partial T}{\partial t} - \boldsymbol{V}^{\mathrm{FTALE}} \cdot \operatorname{grad} T \right) + k \operatorname{grad} \delta T|_{\Gamma_{SL}} \cdot \operatorname{grad} T \right\} ds \\
&\qquad - \int_{\partial\Omega} k \delta T|_{\Gamma_{SL}} \frac{\partial T}{\partial n} \, dl
\end{aligned} \tag{25}$$

and the velocities of the interface points are obtained by solving the algebraic system

$$[\mathrm{M}^{\mathrm{SL}}]\{\mathrm{V}^{\mathrm{SL}}\} = \{\mathrm{F}^{\mathrm{SL}}\}. \tag{26}$$

Here $\{\mathrm{V}^{\mathrm{SL}}\}$ is the vector containing the nodal values of the interface velocity for all the domain nodes located on the liquid–solid interface. $[\mathrm{M}^{\mathrm{SL}}]$ is the mass matrix for the L2 elements and is given by

$$M_{ij}^{SL} = \int_{\Gamma_{SL}} \rho^- \Delta H \Phi_i \Phi_j \, dl, \tag{27}$$

where Φ_i are the L2 finite element bases. $\{\mathrm{F}^{\mathrm{SL}}\}$ is the vector containing the thermal equivalent of the nodal reaction forces. It is obtained by assembling the residuals of the nodes located on Γ^{SL}, by postprocessing the heat transfer problem.

Lynch and Sullivan [31] have shown that calculation of the phase boundary motion in this way leads to a perfect heat balance and yields second-order accuracy overall. However, in applying this method we have observed spurious oscillations of the liquid–solid interface. These oscillations arise from the anisotropy of the triangular elements, as can be seen from a simple example. Consider a mesh of equal-size T3 elements like that in Fig. 16b. Assume that an initially flat solidification front propagates from the left to the right, starting at the left boundary ($x = 10$ in Fig. 16b). The nodes located on the solidification front are then of two kinds, according to the number of surrounding elements that contribute to the determination of the normal heat flux (two or four). This yields a small difference in the computed normal heat flux, and thus on the predicted front velocity, for the two classes of nodes. Since nodes of each kind are arranged alternately along the interface, an oscillation of the front is generated, with a length scale proportional to the element size and an amplitude that increases with the magnitude of the time step. This origin of the spurious oscillations can be checked easily by orienting the longest edge of all the T3 elements in the same

direction. In this case, no oscillation is produced along the front. Indeed, all nodes are then topologically similar. Unfortunately, such a simple trick cannot be used in the general case. Moreover, it introduces a global asymmetry of the mesh (nodes located on two opposite boundaries of the mesh are not equivalent).

Smoothing can be achieved by using a lumped mass matrix instead of the consistent mass matrix (27), but the oscillations remain. A straightforward analysis of the problem indicates that the small-scale perturbation induced by the mesh must be removed in a heat-conserving way. To achieve this a diffusionlike term is added to (26). The resultant algebraic system is

$$([\mathrm{M}^{\mathrm{SL}}] + [\mathrm{K}^{\mathrm{SL}}])\{\mathrm{V}^{\mathrm{SL}}\} = \{\mathrm{F}^{\mathrm{SL}}\}, \tag{28}$$

where the diffusion matrix $[\mathrm{K}^{\mathrm{SL}}]$ is given by

$$K_{ij}^{SL} = \int_{\Gamma_{SL}} D^{SL} \frac{d\Phi_i}{dl} \frac{d\Phi_j}{dl}\, dl. \tag{29}$$

Clearly the artificial diffusion coefficient D^{SL} provides the means of controlling the damping. The matrix $[\mathrm{K}^{\mathrm{SL}}]$ acts as a modification to the consistent mass matrix. Note that for $D^{SL} = \rho^{-} \Delta H h^2/6$, where h is the element size, the effective mass matrix $([\mathrm{M}^{\mathrm{SL}}] + [\mathrm{K}^{\mathrm{SL}}])$ is equivalent to the lumped mass matrix.

4. NUMERICAL STUDY

4.1. Assessment of the Osmotic Simulation Capability

The ability of the model to simulate the osmotic response of cells was exploited in [35] to study the behavior of one cell in a salt solution (water + NaCl) with a constant solute concentration gradient. This is a simplification of the situation encountered ahead of an advancing ice front, due to the rejection of the solute by the ice. It is, however, the most realistic configuration to be used in modeling the cryopreservation of cell suspensions. Indeed, most studies in this field have been limited to the uniform distribution case [36] (see [37] for a review). Recently Batycky and co-workers [30] included spatial variation of the solute concentration assuming spherical symmetry. The method described here was used to examine the motion of a cell in a linear solute gradient. Neglecting all other phenomena that may induce a cell motion, e.g., buoyancy or surface energy variations, this study has revealed a plausible mechanism for cell migration toward regions of lower concentration. In the limiting case of very fast diffusion of solute inside and outside the cell, a very simple semianalytical model can be obtained which provides good agreement with our finite element model. However, the method was not described in [35] and a convergence study of the method was lacking.

A schematic of the system is shown in Fig. 5. We consider a circular cell (initial radius r_0) in a rectangular domain filled with a binary solution. The surrounding solute concentration field is characterized by a negative constant gradient $-G$ in the x direction. (In this case we assume an isothermal solution.) Since the external osmotic pressure is higher

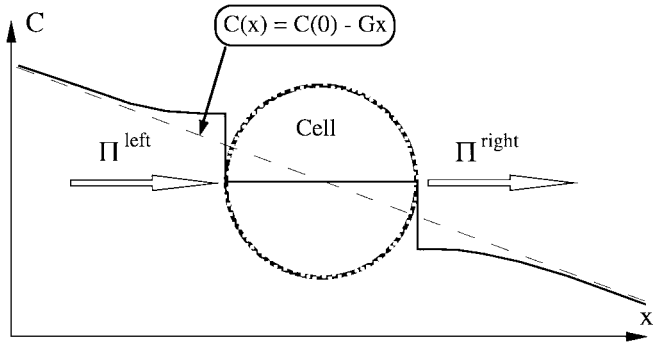

FIG. 5. Schematic of the action of a constant solute concentration gradient on a cell (Π is the osmotic pressure; C is the solute concentration).

on the left side of the cell than on the right side, the cell moves slowly in the x direction, toward the region of lower solute concentration. Simultaneously, its size increases as the mean external concentration decreases. When the internal concentration C_0 is initially lower than the corresponding external value (hypertonic environment) or higher (hypotonic environment), the cell migration is preceded by a rapid shrinkage or swelling of the cell, respectively.

In the case of fast diffusion (much faster than the motion of the cell), the concentration inside the cell is uniform and the external concentration gradient is determined by a solution of the Laplace equation with zero normal gradient at the cell boundary and a constant gradient far from the cell. The evolution of the cell centroid x_c and cell radius r is then given by

$$\frac{dx_c}{dt} = 2LRTGr, \tag{30}$$

$$\frac{dr}{dt} = -LRT\left(C_f(0) - Gx_c - C_0\left(\frac{r_0}{r}\right)^2\right), \tag{31}$$

where $C_f(0)$ is the undisturbed fluid concentration at $x = 0$.

For the convergence study, the isotonic case has been considered with a domain of 100×50 μm and an initial cell radius of 5 μm. Exploiting the symmetry of the problem about the x axis, the computation can be restricted to a half domain containing a half cell. The set of equations to be solved included the diffusion equation (12) with the interfacial conditions (13) and (15). A zero flux has been imposed along the upper and lower boundaries. The solute concentration was fixed to its analytical far field values at the right and left boundaries. The values of G, L, R, and T were set to 0.01 M/μm, 10 μm/mn $\cdot$ atm, 0.08206 atm/M $\cdot$ K, and 273 K respectively, which correspond to realistic physical values. The diffusion coefficients in the cell and ambient fluid were assumed equal ($D = 10^6$ μm^2/s). The domain was decomposed into three regions: an inner cell region (30 μm) and two outer ones (35 μm each). The two outer regions were discretized with 10 proportionally spaced T3 elements in the x direction while the cell region was refined using equally spaced T3 elements. Eight different grid resolutions were considered for the inner region. Figure 6 shows a close-up of the inner region for the 30×26 grid after the domain mesh was adapted to the membrane location at time $t = 15$ s. In all cases the membrane mesh had 60 L2 elements.

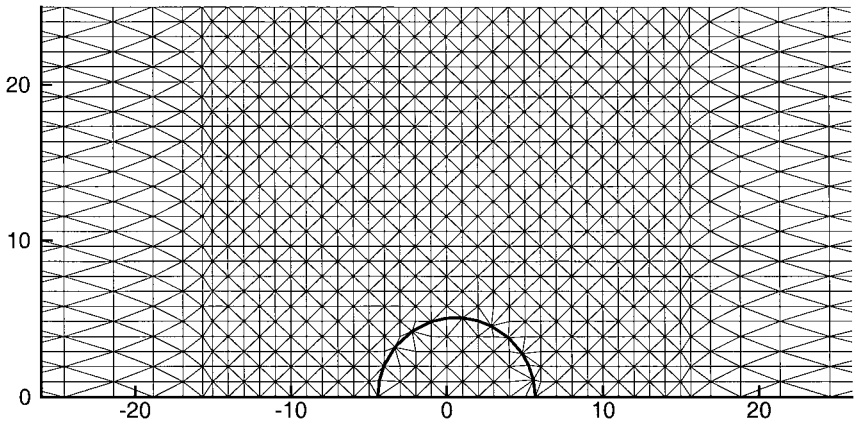

FIG. 6. Mesh in the cell region for the 30×26 grid resolution after adaptation to the membrane location ($t = 15$ s).

A comparison of the computed results and the analytical model can be found in Fig. 7, where we have plotted the evolution of the cell radius and cell centroid in nondimensional variables for four different grid resolutions in the cell region. The numerical results obtained with the 30×26 grid resolution are in good agreement with the analytical solution.

In order to determine the rate of spatial convergence, we have plotted in Fig. 8 two quantities that characterize the improvement of the predicted cell centroid location $x_c(N_i)$ and cell radius $r(N_i)$ with mesh refinement. The numerical model exhibits a near quadratic convergence for both quantities. Refining the 30×26 mesh once more leads to a change

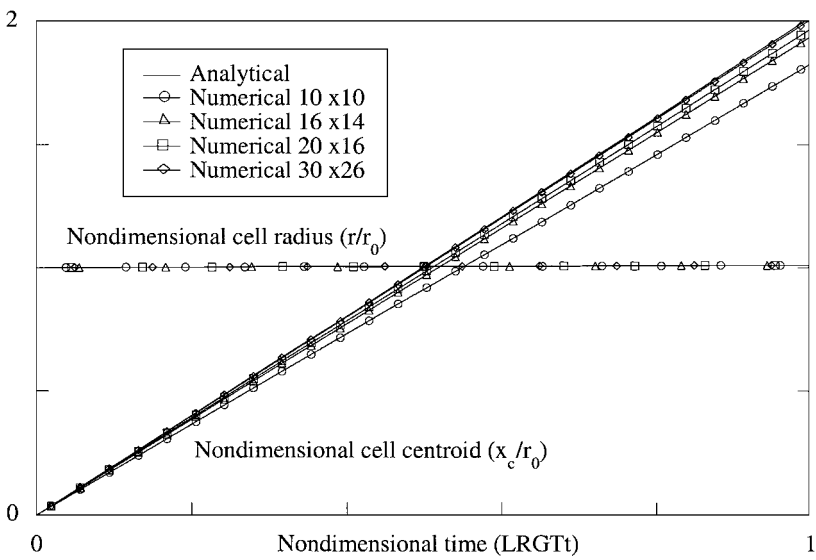

FIG. 7. Osmotic response of a cell in a constant solute concentration gradient ($\Delta t = 0.01$ s for all grid resolutions).

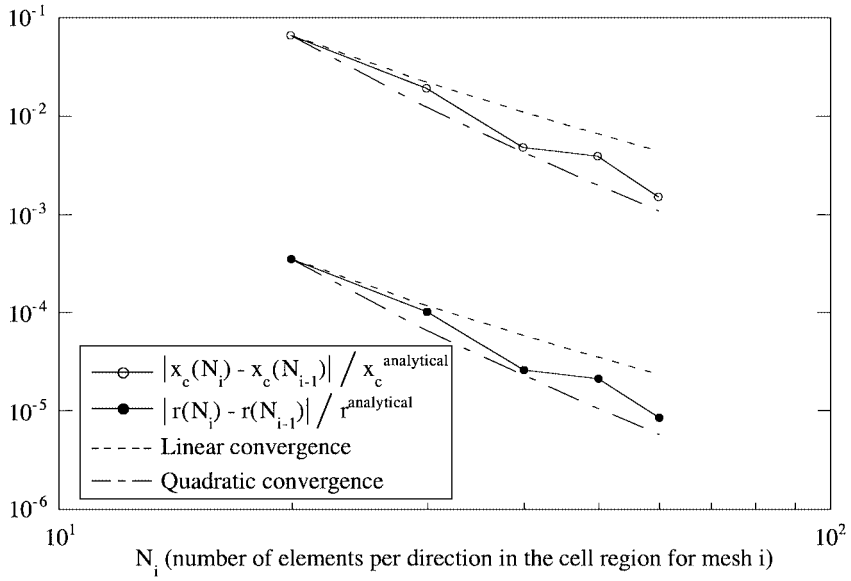

FIG. 8. Spatial convergence for the osmotic migration problem ($LRTGt = 0.5$, $\Delta t = 0.01$ s). Subscript i corresponds to five successive mesh refinements (20×16, 30×26, 40×30, 50×40, and 60×50) of an initial 10×10 grid resolution of the cell region.

in the solution of less than 0.5% for the cell centroid location and less than 0.003% for the cell radius.

The first-order backward difference scheme leads to a linear convergence in time, as illustrated in Fig. 9. For time steps smaller than $\Delta t = 0.012$ s the change in the predicted cell centroid location is insignificant (<0.0002%).

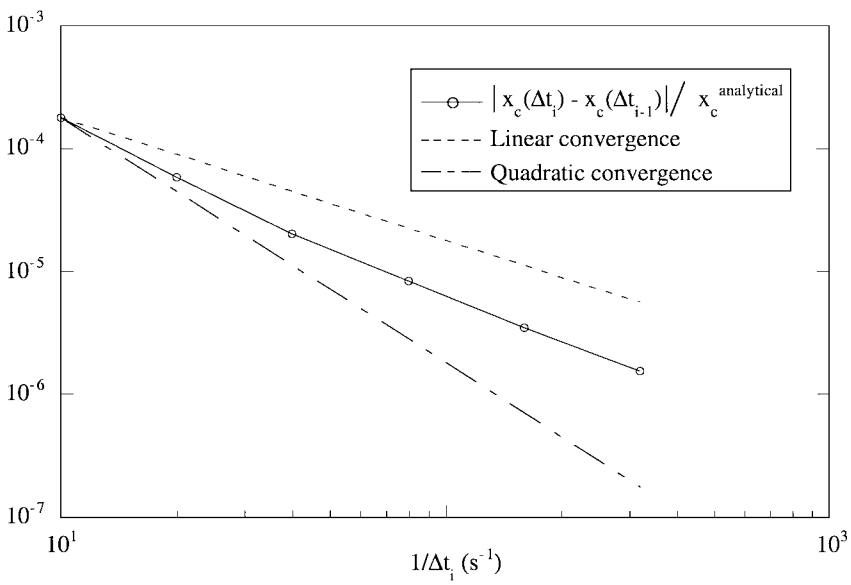

FIG. 9. Temporal convergence for the osmotic migration problem ($LRTGt = 0.5$, 60×50 grid resolution). Subscript i corresponds to six successive time-step refinements ($\Delta t_i = t_{i-1}/2$ with $\Delta t_0 = 0.1$ s).

4.2. Assessment of the Phase-Change Capability of the Method

4.2.1. *Validation with an Exact Analytical Solution of a Stefan Problem*

A few analytical solutions are available for a class of freezing problems referred to as Stefan problems. They describe the solidification of a melt or the melting of a solid in a simplified one-dimensional, cylindrical, or spherical geometry [38]. We selected the growth of a cylindrical solid from its supercooled pure melt for the validation of our numerical model. This problem is governed by Eq. (11) with the interfacial condition (17). The temperature of the solidification front is given by a simplified version of (19), in which the Gibbs–Thomson and kinetic effects are neglected. Thus, the temperature of the solidification front is simply equal to the equilibrium melting temperature T_m. In terms of the nondimensional variables

$$\theta = C_P^-(T - T_m)/\Delta H, \quad \tilde{l} = l/l_{\text{ref}}, \quad \tilde{t} = tk^-/\rho C_P^- l_{\text{ref}}^2, \quad \text{and} \quad \tilde{V} = V\rho C_P^- l_{\text{ref}}/k^-,$$

where l_{ref} is a suitable length scale, the set of equations to be solved becomes

$$\left(\frac{C_P}{C_P^-}\right)\frac{\partial\theta}{\partial\tilde{t}} = \text{div}\left(\left(\frac{k}{k^-}\right)\text{grad}\,\theta\right), \tag{32}$$

$$\tilde{V}^{SL} = \left(\frac{\partial\theta}{\partial n}\right)^- - \left(\frac{k^+}{k^-}\right)\left(\frac{\partial\theta}{\partial n}\right)^+, \tag{33}$$

$$\theta^{SL} = 0. \tag{34}$$

The strength of the undercooling is given by the value of the temperature at infinity or by the Stefan number $\text{St} = \theta_\infty = C_P^-(T_\infty - T_m)/\Delta H$. Because of the axial symmetry of the problem, these equations can be solved analytically in 1D cylindrical coordinates (r, t) to yield the solution [38]

$$\theta(\tilde{r}, \tilde{t}) = 0 \quad \text{if } \tilde{r} \le \tilde{r}^{SL}(\text{liquid}), \tag{35}$$

$$\theta(\tilde{r}, \tilde{t}) = \text{St}\left(1 - \frac{Ei\left(-\left(\frac{k^-C_P^+}{k^+C_P^-}\right)\frac{\tilde{r}^2}{4\tilde{t}}\right)}{Ei(-\lambda^2)}\right) \quad \text{if } \tilde{r} \ge \tilde{r}^{SL}(\text{solid}), \tag{36}$$

$$\tilde{r}^{SL}(\tilde{t}) = 2\lambda\sqrt{\left(\frac{k^+C_P^-}{k^-C_P^+}\right)\tilde{t}}, \tag{37}$$

where Ei is the exponential integral and λ is the root of

$$\lambda^2 e^{\lambda^2} Ei(-\lambda^2) - \left(\frac{C_P^+}{C_P^-}\right)\text{St} = 0. \tag{38}$$

The finite element model has been applied to (32)–(34) using 2D Cartesian coordinates on a unit square centered at the origin. The initial and boundary conditions corresponded to those of the exact solution. The computations were started with an initial nondimensional radius of the solid phase of 0.1 and were stopped when the solid cylinder reached a nondimensional radius of 0.4. Computations were undertaken for two values of the Stefan

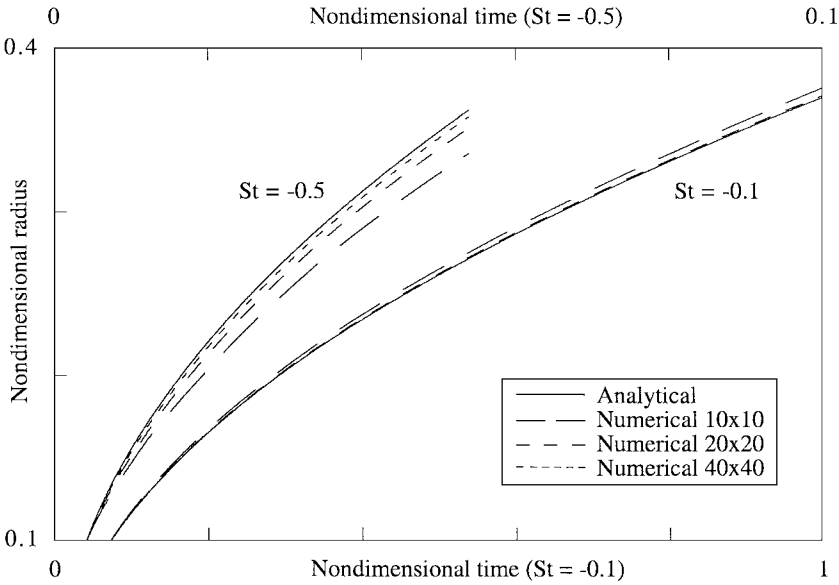

FIG. 10. Growth of a cylinder in its undercooled melt: evolution of the cylinder radius ($\Delta t/t_{\text{ref}} = 0.001$ for $\text{St} = -0.1$ and $\Delta t/t_{\text{ref}} = 0.0001$ for $\text{St} = -0.5$).

number: equal physical properties between the solid and liquid phases and a unit latent heat of fusion. A uniform mesh with eight different grid resolutions has been used. Initially, the interface mesh had 100 L2 elements (LBH = 0.1 and UBH = 0.5). A variation of less than 0.1% was observed in the predicted radius of the solid region over the set of interface nodes for each grid resolution and at each time step. The time evolution of the mean radius is plotted in Fig. 10. Convergence to the analytical solution is seen for both values of the Stefan number (St). For $\text{St} = -0.1$, the curves corresponding to the analytical solution and to the numerical solution obtained with the 50×50 mesh are superimposed. For $\text{St} = -0.5$, this occurs only for the 80×80 and finer grid resolutions.

The artificial diffusion coefficient D^{SL} used in the weak formulation of the Stefan condition (as described in Section 3.2.4) was set to 0.01 for all computations. With a smaller value, the solidification front starts to produce oscillations. To appreciate the magnitude of the modification introduced to the consistent mass matrix, consider that a value of 0.002 would correspond to the lumped mass matrix for the 10×10 grid resolution.

The rate of spatial convergence is illustrated in Fig. 11. The numerical model exhibits a quadratic convergence. Refining the 40×40 mesh once more leads to a change in the radius of less than 0.05%.

The linear convergence of the temporal scheme is illustrated in Fig. 12. Refining the $\Delta t/t_{\text{ref}} = 0.001$ time step once more leads to a change in the predicted radius of less than 0.02%.

In order to demonstrate the ability of the model to deal with discontinuous material properties, we computed the same problem in the case of water for $\text{St} = -0.1$. The difference in material properties between the liquid and solid phases is given by $C_P^-/C_P^+ = 1.98$ and $k^-/k^+ = 0.266$, which corresponds to a biological solution of salt water. The predicted temperature profiles are compared to the exact solution in Fig. 13. Very good agreement can be seen in this plot.

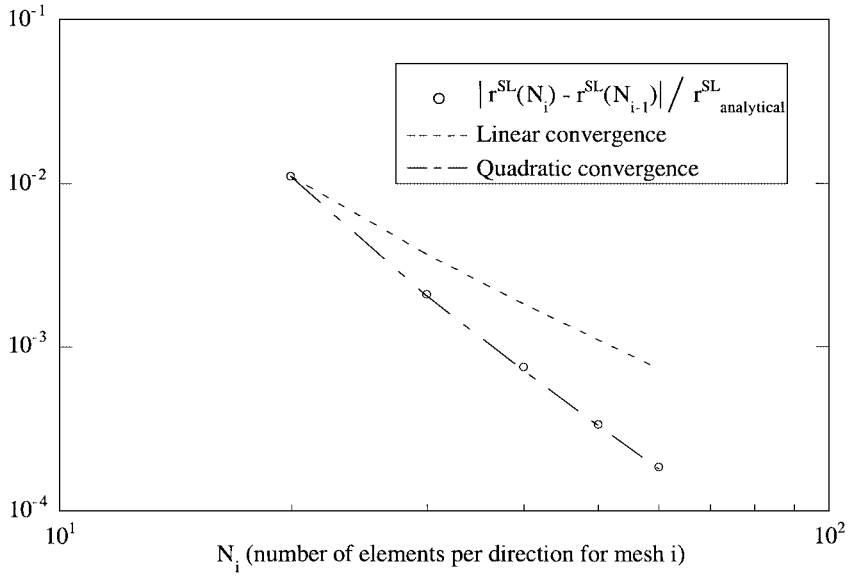

FIG. 11. Spatial convergence for the supercooled Stefan problem ($\mathrm{St} = -0.1$, $t/t_{\mathrm{ref}} = 0.5$). $r^{SL}(N_i)$ is the radius of the solid phase. Subscript i corresponds to five successive mesh refinements (20×20, 30×30, 40×40, 50×50, and 60×60) of an initial 10×10 grid resolution.

Finally, in order to show that the model is insensitive to the orientation of the element mesh, we considered a case using the unstructured mesh shown in Fig. 14. The results obtained are in very good agreement with the analytical solution, as seen in Fig. 15, where the evolution of the nondimensional radius of the solid phase is plotted.

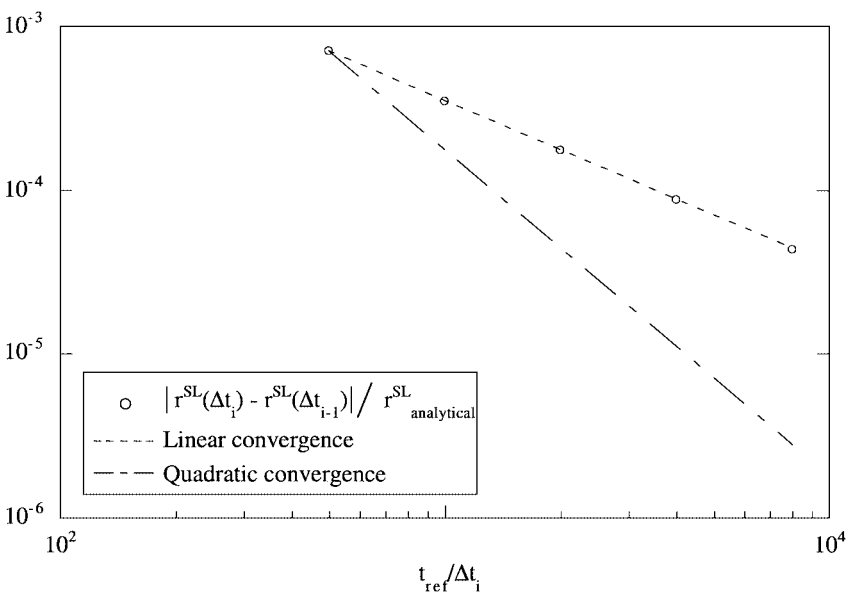

FIG. 12. Temporal convergence for the supercooled Stefan problem ($\mathrm{St} = -0.1$, $t/t_{\mathrm{ref}} = 0.5$). Subscript i corresponds to five successive time-step refinements ($\Delta t_i = \Delta t_{i-1}/2$ with $\Delta t_0/t_{\mathrm{ref}} = 0.002$).

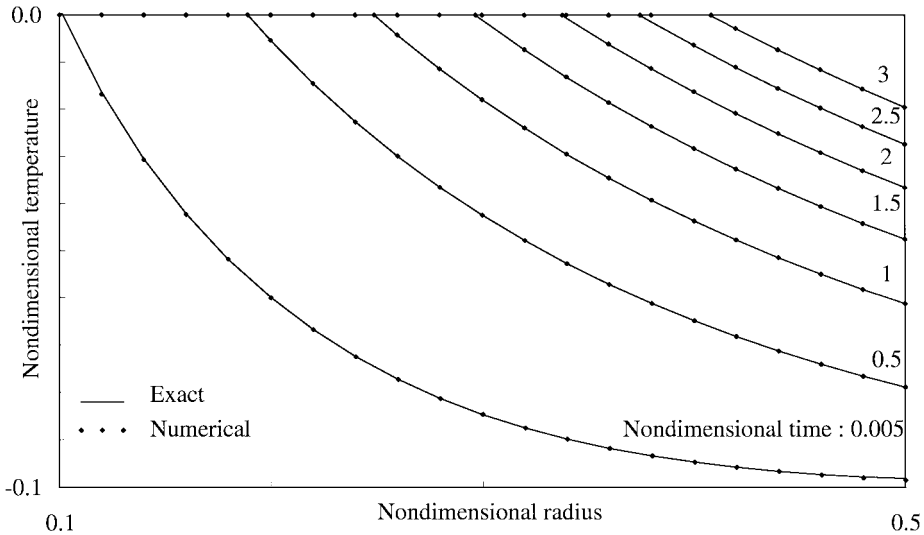

FIG. 13. Growth of a cylinder of ice in undercooled water (50×50 grid resolution, $\Delta t / t_{\text{ref}} = 0.0005$).

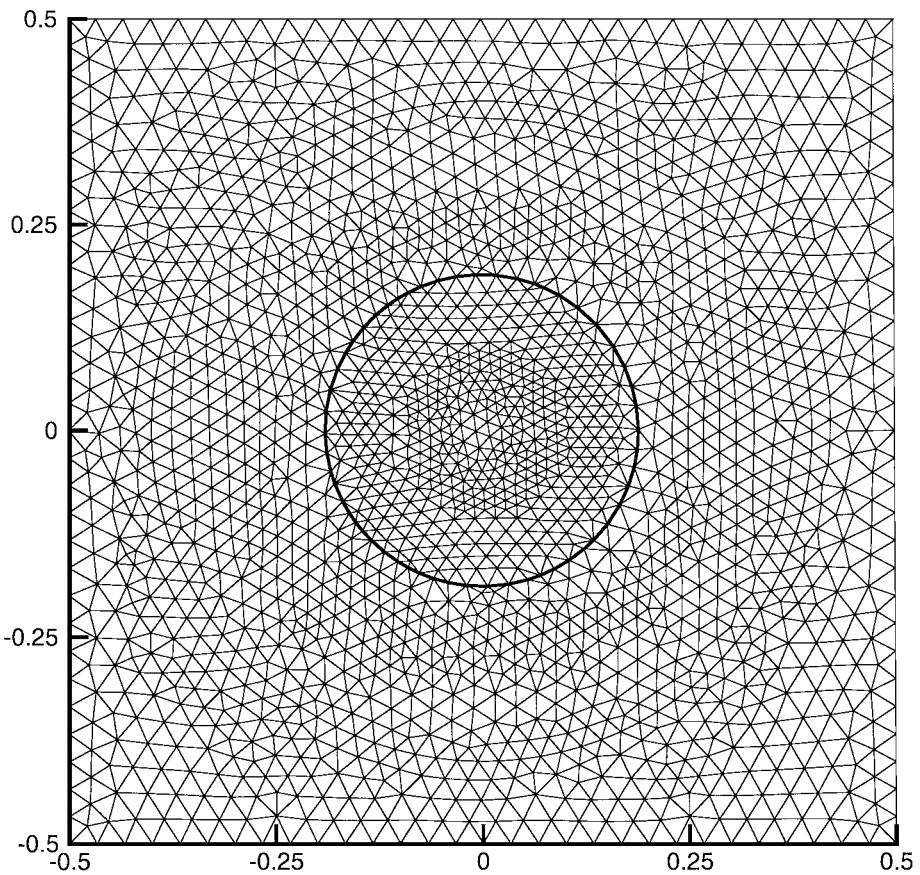

FIG. 14. Unstructured mesh (3810 T3, 1966 domain nodes) for the computation of the supercooled Stefan problem for water. The black circle corresponds to the location of the ice front at this time.

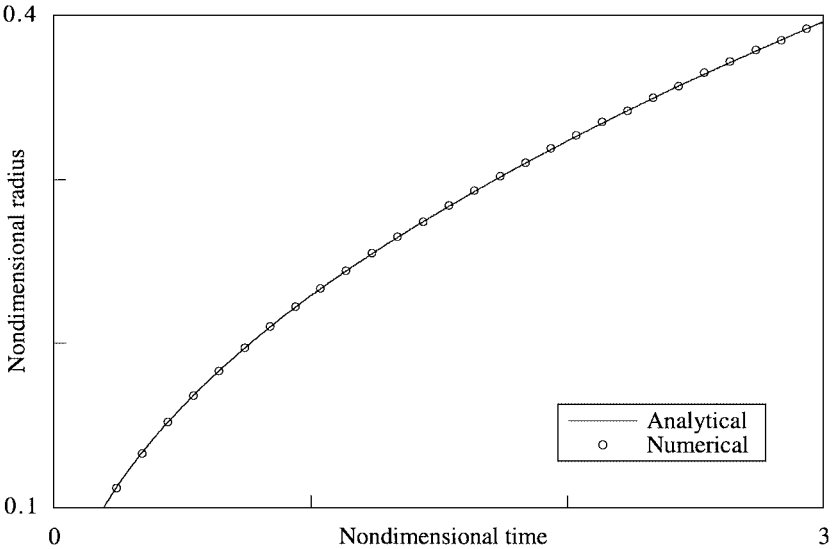

FIG. 15. Growth of a cylinder of ice in undercooled water. Average radius, obtained with the unstructered mesh of Fig. 14, versus time.

4.2.2. *Ability to Simulate Unstable Growth*

In the absence of any surface tension effect, the growth of a cylindrical solid in its undercooled pure melt is unstable relative to perturbations of any wave length. It is clear that the artificial diffusion coefficient D^{SL}, introduced in the weak formulation of the Stefan condition, must act as a stabilizing force on the solidification front. The following question arises: When the Gibbs–Thomson effect is taken into account in the analysis, can this coefficient be reduced sufficiently in order to accurately reproduce the instability? To answer this question we explored the instability of a flat solidification front advancing at constant velocity into an undercooled melt. This problem is well documented, both theoretically and numerically.

The set of equations to be solved includes the heat equation (11) with the interfacial conditions (17) and (19). In a frame of reference moving with the interface, this system has a stationary solution with a constant front speed V_{sta}, which we take as the reference velocity. In terms of the nondimensional variables

$$\theta = C_P^+(T - T_m)/\Delta H, \quad \tilde{l} = l/l_{\text{ref}}, \quad \tilde{t} = tV_{\text{sta}}/l_{\text{ref}}, \quad \text{and} \quad \tilde{V} = V/V_{\text{sta}},$$

where l_{ref} is a suitable length scale, the set of equations to be solved becomes

$$\frac{\partial\theta}{\partial\tilde{t}} = \frac{1}{\text{Pe}_T}\Delta\theta \quad \text{with } \text{Pe}_T = \frac{l_{\text{ref}}V_{\text{sta}}}{k/\rho C_P}, \tag{39}$$

$$\tilde{V}^{SL} = \frac{1}{\text{Pe}_T^+}\left(\left(\frac{k^-}{k^+}\right)\left(\frac{\partial\theta}{\partial n}\right)^- - \left(\frac{\partial\theta}{\partial n}\right)^+\right), \tag{40}$$

$$\theta^{SL} = -\left(\frac{d_0}{l_{\text{ref}}}\right)\tilde{\kappa} - \left(\frac{V_{\text{stat}}C_P^+}{\mu\Delta H}\right)\tilde{V}^{SL}. \tag{41}$$

In these equations Pe_T is a thermal Peclet number and $d_0 = \gamma T_m C_P^+ / \rho \Delta H^2$ is a capillary length. The degree of undercooling is given by the value of the temperature at infinity or by the Stefan number $\mathrm{St} = \theta_\infty = C_P^+ (T_\infty - T_m)/\Delta H$.

For a front moving in the x direction, the steady-state planar solution is given by

$$\theta(\tilde{x}, \tilde{t}) = 0 \quad \text{if } \tilde{x} \le \tilde{x}^{SL} \text{ (liquid)}, \tag{42}$$

$$\theta(\tilde{x}, \tilde{t}) = \exp(-\mathrm{Pe}_T^+ (\tilde{x} - \tilde{x}^{SL})) + \theta_\infty \quad \text{if } \tilde{x} \ge \tilde{x}^{SL} \text{ (solid)}, \tag{43}$$

$$V_{\mathrm{sta}} = -\left(\frac{\mu \Delta H}{C_P^+} \right) (1 + \theta_\infty). \tag{44}$$

The kinetic coefficient μ is positive, and the solution exists only for Stefan numbers smaller than -1. For $\mathrm{St} = -1$, the steady-state front speed becomes indeterminent since the right hand side of (44) vanishes. Neglecting the kinetic effect contribution in (41) means that μ is infinite, implying an infinite front speed. In this case, $\mathrm{St} = -1$ is the only possible value for which a planar steady-state solution can exist. A physical description of the instability process and a linear stability analysis for this last situation can be found in [39]. A numerical study extending to the nonlinear regime has been reported by Sullivan and co-workers using finite elements with moving meshes [40, 41]. Here we also consider this last configuration, thus setting θ_∞ to -1 in (43) and (44), with a unit steady-state front speed ($V_{\mathrm{sta}} = 1$). The linear stability analysis predicts that the interface is unstable to any perturbation of wavelength λ greater than

$$\lambda_S = 2\pi \sqrt{1 + K^-/k^+} \sqrt{d_0 \rho C_P^+ / k^+}. \tag{45}$$

The fastest growing wavelength is $\lambda_{\max} = \sqrt{3}\lambda_S$. This wavelength has been chosen as the reference length scale ($l_{\mathrm{ref}} = \lambda_{\max}$) for the numerical study. The material properties are $\rho C_P^- = \rho C_P^+ = 1$, $k^- = 0$, and $k^+ = 100$. The value of the capillary length d_0 can be deduced from (45) in order to select a specified value for the wavelength λ_S.

As in the osmotic study, the domain contains an inner region with equally spaced elements corresponding to the zone where the interface evolves and two outer regions with proportionally spaced elements. The inner region has a length of 2 whereas the left and right outer regions have lengths of 10 and 400, respectively. The left and right boundaries can be assumed to be in the far field and constant temperatures can be specified there ($\theta_{-\infty} = 0$ and $\theta_{+\infty} = -1$). The domain in the y direction, perpendicular to the front motion, extends from -1 to 1 in order to simulate the growth of two wavelengths of the fastest growing perturbation. A zero flux condition has been imposed along the upper and lower boundaries. The mesh in the inner region consists of 3200 equal-size T3 elements and yields a 40×40 grid resolution. Eight hundred T3 elements were used for both outer regions. The interface mesh had 100 L2 elements (LBH = 0.3 and UBH = 0.6).

The computations were initiated with a temperature field corresponding to the steady-state solution and the following small perturbation of the front shape:

$$\xi_0(\tilde{y}) = A_0(\cos(2\pi\tilde{y}) + \cos(4\pi\tilde{y})). \tag{46}$$

The initial amplitude A_0 is identical for both waves and equal to 0.005. This system has been studied using different values for the diffusion coefficient D^{SL}. Clearly, large values

TABLE I
Error on the Amplification of the Perturbation Relative to the Case $D^{SL} = 0$

	$D^{SL} = 1$	$D^{SL} = 0.1$	$D^{SL} = 0.01$	$D^{SL} = 0.001$	$D^{SL} = 0.0001$
$\Delta\tilde{t} = 0.005$	94%	59%	11%	Divergence	Divergence
$\Delta\tilde{t} = 0.001$	94%	59%	11%	1%	Divergence
$\Delta\tilde{t} = 0.0001$	94%	59%	11%	1%	0.1%

Note. Error (%) $= \dfrac{\Delta A(D^{SL}) - \Delta A(D^{SL} = 0)}{\Delta A(D^{SL} = 0)}$ with $\Delta A = A(t/t_{\text{ref}} = 0.2) - A(t/t_{\text{ref}} = 0.1)$.

(on the order of 0.1 and greater) limit the development of the instability. However, in all cases, the numerical model selects the right wavelength, and for the smaller values of D^{SL}, bifurcation to cellular crystal growth occurred. Convergent results could also been obtained with $D^{SL} = 0$ but smaller time steps were needed. (The maximum value of the time step that can be used decreases with D^{SL}.) The stabilizing effect of D^{SL} is quantified in Table I for decreasing values of the nondimensional time step.

The ability of the method to simulate the cellular crystal growth for a longer period has been checked for one dendrite. To do this, the size of the computational domain in the y direction has been divided by two in order to simulate just one wavelength and the length of the inner region has been multiplied by five. A mesh of 200×20 equally spaced T3 elements in this region ensured the same grid resolution as previously used. The evolution of the front shape and the computational mesh in the inner region are plotted in Fig. 16. The finger-shaped dendrite obtained compares well with those reported in [40].

4.3. Application to the Interaction of One Cell with an Ice Front

Our study of the osmotic response of a cell during freezing was limited to the early stage, where an advancing solidification front approaches the cell [35]. We assumed that the front remains flat until it reaches the cell, after which the analyses broke down. The extension of the method to handle phase change allows us to examine the later solidification stage, where the cell is engulfed in the solid phase.

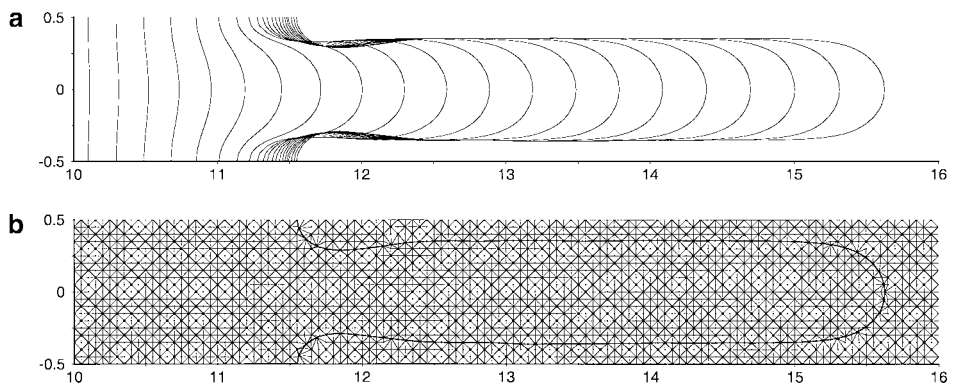

FIG. 16. Computed cellular crystal growth ($D^{SL} = 0.01$, $\Delta t/t_{\text{ref}} = 0.002$.) (a) Evolution of the solidification front (equal nondimensional time intervals of 0.2); (b) domain mesh in the inner region, adapted to the interface location ($t/t_{\text{ref}} = 4$).

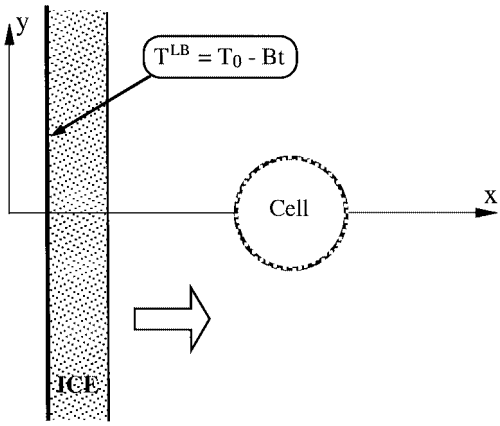

FIG. 17. Interaction of one cell with an ice front: initial configuration.

The configuration to be analyzed here is sketched in Fig. 17. The freezing is driven from the left boundary, at which the temperature T^{LB} is decreased at a constant cooling rate B. As the temperature of the system decreases, a flat ice front, initially close to this boundary, advances toward a cell located initially at a given distance from the front. The initial temperature of the system is uniform and equal to $T_0 = T_m + mC_0$, where C_0 is the initial solute concentration of the liquid phase inside and outside of the cell (isotonic case).

The set of equations governing this problem is the full set of equations presented in Section 3.1. In terms of the nondimensional variables

$$\theta = C_P^+(T - T_0)/\Delta H, \quad \tilde{C} = (C - C_0)/C_0, \quad \tilde{l} = l/l_{\mathrm{ref}}, \quad \tilde{t} = tV_{\mathrm{ref}}/l_{\mathrm{ref}}, \quad \text{and} \quad \tilde{V} = V/V_{\mathrm{ref}},$$

where l_{ref} and V_{ref} are suitable length and velocity scales, this set of equations becomes

$$\frac{\partial\theta}{\partial\tilde{t}} = \frac{1}{\mathrm{Pe}_T}\Delta\theta \quad \text{with } \mathrm{Pe}_T = \frac{l_{\mathrm{ref}}V_{\mathrm{ref}}}{k/\rho C_P}, \tag{47}$$

$$\frac{\partial\tilde{C}}{\partial\tilde{t}} = \frac{1}{\mathrm{Pe}_C}\Delta\tilde{C} \quad \text{with } \mathrm{Pe}_C = \frac{l_{\mathrm{ref}}V_{\mathrm{ref}}}{D}, \tag{48}$$

$$\tilde{V}^{SL} = \frac{1}{\mathrm{Pe}_T^+}\left(\left(\frac{k^-}{k^+}\right)\left(\frac{\partial\theta}{\partial n}\right)^- - \left(\frac{\partial\theta}{\partial n}\right)^+\right), \tag{49}$$

$$\tilde{V}^{CL} = -\left(\frac{LRT_0C_0}{V_{\mathrm{ref}}}\right)\left(1 + \frac{\theta\Delta H}{T_0C_P^+}\right)(\tilde{C}^+ - \tilde{C}^-), \tag{50}$$

$$\theta^{SL} = \left(\frac{mC_0C_P^+}{\Delta H}\right)\tilde{C} - \left(\frac{d_0}{l_{\mathrm{ref}}}\right)\tilde{\kappa} - \left(\frac{V_{\mathrm{ref}}C_P^+}{\mu\Delta H}\right)\tilde{V}^{SL}, \tag{51}$$

$$\frac{1}{\mathrm{Pe}_C^{\pm}}\left(\frac{\partial\tilde{C}}{\partial n}\right)^{\pm} = (1 - \tilde{C}^{\pm})\tilde{V}^{CL} \quad \text{on } \Gamma_{CL}, \tag{52}$$

$$\frac{1}{\mathrm{Pe}_C^+}\left(\frac{\partial\tilde{C}}{\partial n}\right)^{+} = (1 - \tilde{C}^{+})\tilde{V}^{SL} \quad \text{on } \Gamma_{SL}, \tag{53}$$

TABLE II
Physical Properties Used for the Analysis of the Engulfment of One Cell

	ρ (kg/m^3)	C_P (J/kg · K)	k (W/m · K)	D (m^2/s)	T_m (K)	m (K/M)	ΔH (J/kg)	γ (J/m^2)
Liquid	1000	4200	0.588	7.8×10^{-10}	273.15	−3.72	333×10^3	0.01598
Solid	1000	2120	2.21					

where Pe_T and Pe_C are thermal and solute Peclet numbers and d_0 is a capillary number defined as in Section 4.2.2. The left boundary condition becomes

$$\theta^{\mathrm{LB}} = -\beta\tilde{t}, \tag{54}$$

where $\beta = Bt_{\mathrm{ref}}C_p^+/\Delta H$ is a nondimensional parameter.

As in the numerical study of Section 4.1., we considered the case of a salt solution with the physical properties given in Table II. The contribution of the kinetic effect to the definition of the front temperature was neglected.

A preliminary series of computations without any cell in the system has shown that the solidification front rapidly assumes a quasiconstant speed whose magnitude depends on the value of the cooling rate [29]. The front velocities predicted by our model for $B = 0.05$, 0.1, and 0.2 K/s, as well as the solute concentration profiles ahead of the front, agreed well with the results obtained in [42].

The engulfment of one cell was studied with a cooling rate of 0.1 K/s. The front speed in the absence of a cell was taken as the reference velocity scale ($V_{\mathrm{ref}} = 10$ μm/s) and the initial cell radius as the reference length scale ($l_{\mathrm{ref}} = r_0 = 5$ μm). The initial solute concentration C_0 was set to 0.154 M, which yields an initial temperature T_0 equal to 272.58 K. The permeability of red blood cells were used ($L_{\mathrm{ref}} = 10$ μm/mn · atm, $T_{\mathrm{ref}} = 296$ K, $R = 0.08206$ atm/M · K, and $E = 16300$ J/mol in (14)). The cell centroid was initially at a distance of 52.5 μm from the ice front, which was initially located 2.5 μm from the left boundary. The computational domain was a 2D rectangle of 530×20 μm. We computed this case with an unstructured mesh consisting of 2458 T3 elements and 1326 domain nodes. The membrane mesh had 60 L2 elements, and the solidification front mesh initially had 20 L2 elements.

The aim of this computation was to study the interaction of a cell and an initial planar solidification front. Therefore, during the first stage, where the front approaches the cell, the diffusion coefficient D^{SL} was set to a large value ($D^{SL} = 100$) in order to save computational time. Twelve thousand nondimensional time steps of 10^{-3} were required to compute this early stage. The diffusion coefficient was reduced ($D^{SL} = 0.01$) in order to study the front shape evolution. Fifty thousand nondimensional time steps of 5×10^{-5} followed by 80,000 time steps of 25×10^{-6} and 50,000 time steps of 125×10^{-7} were required to compute this second stage. Figure 18a shows the evolution of the solidification front and the cell membrane. The mesh in the cell region after adaptation is displayed in Fig. 18b. It can be seen that the presence of a cell in the liquid phase causes the liquid–solid interface to become concave as the solidification front approaches the cell. The latter is due to the lowering of the melting point as the solute concentrates in the gap between the cell and the front.

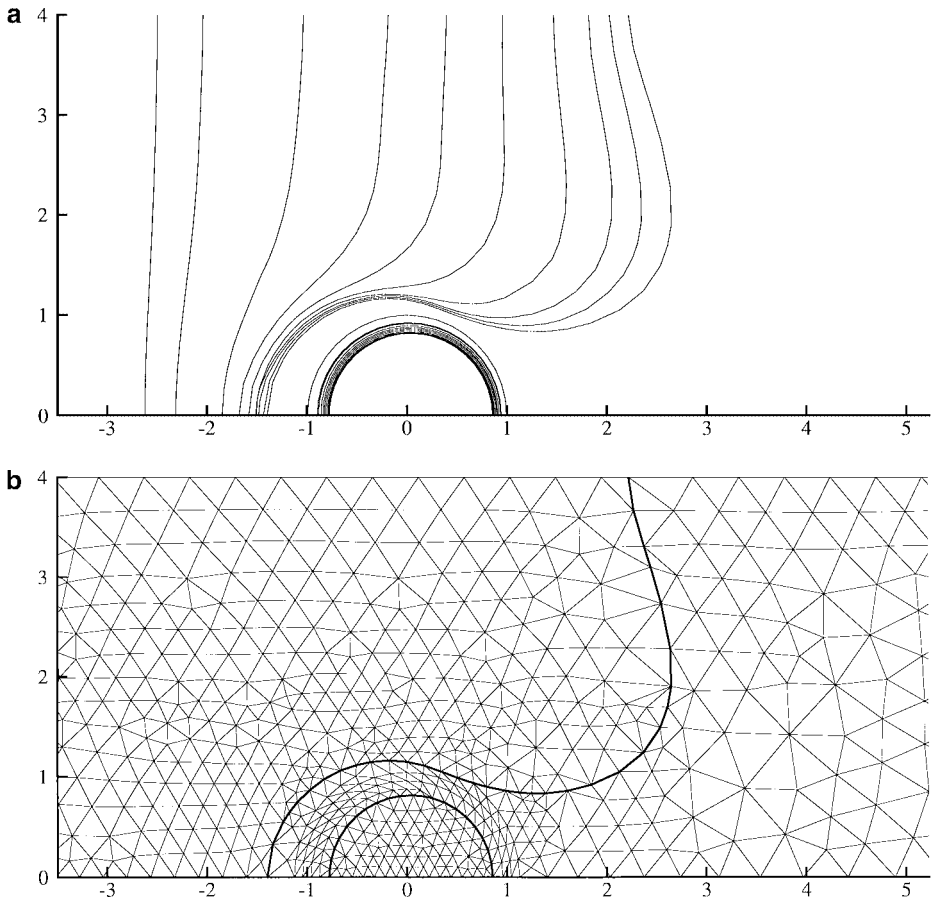

FIG. 18. Engulfment of a cell in an advancing ice front. (a) Ice front and cell membrane ($t/t_{\text{ref}} = 5$, 12.5, 13, 14, 14.75, 15.25, 15.75, 16.25, 16.625, 16.875, and 17.125); (b) mesh in the cell region after adaptation ($t/t_{\text{ref}} = 17.125$).

In order to study the engulfment process for a longer period we reduced, by a factor of 2, the height of the computational domain. The simulation corresponds to the freezing of a row of cells parallel to the initial planar front separated by a gap of 10 μm. This situation can be encountered during the cryopreservation of a cell suspension. Moreover, in order to see the influence of the initial cell position on the front deformation and the cell response, two simulations were performed, with the cell initially located 52.5 and 97.5 μm from the ice front. In the last case, the computational domain was extended to 575 μm in the x direction. The engulfment of one cell and its subsequent shrinkage are shown in Fig. 19 for both cases. The predicted front deformation is qualitatively consistent with the experimental observations reported by Ishiguro and Rubinsky [43]. However, in making this comparison one has to be very cautious and keep in mind the underlying assumptions of our model: (i) it is 2D, and (ii) it neglects many important physical phenomena, such as convection induced by the density jump at the phase-change front, attractive/repulsive forces between this latter and the cell membrane, and concentration-dependent differences in surface energy. Nevertheless, their results show that ice crystal can grow around red blood cells and lead to the formation of an unfrozen solution channel, as predicted by our

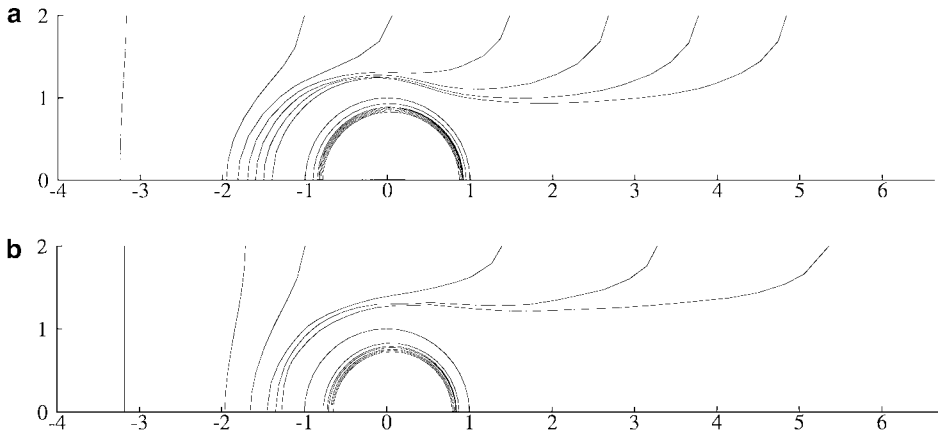

FIG. 19. Engulfment of one cell of a row of cells (separated by a gap of 10 μm). (a) Ice front and cell membrane ($t/t_{ref} = 2$, 12, 14.25, 14.75, 15.25, 15.75, 16.25, and 16.75; initial cell-front distance of 52.5 μm); (b) ice front and cell membrane ($t/t_{ref} = 5$, 22.25, 23.75, 24.25, 25, 25.5, and 26; initial cell-front distance of 97.5 μm).

model. It is worth noting that the computations predict a larger channel width when the initial front-cell distance is increased. Indeed, the enrichment of solute inside the unfrozen solution channel is greater when the solidification front comes from further away, thus constraining the ice to slower growth in this direction.

In Fig. 20, we have plotted the evolution of the solute concentration profile in a cross section through the middle of the cell for an initial distance between the cell centroid and the solidification front of 52.5 μm. It can been seen that the drop in concentration across the cell becomes larger with time since the ambient salt concentration increases too fast for the cell to equilibrate its intracellular concentration with the environment. The concentration

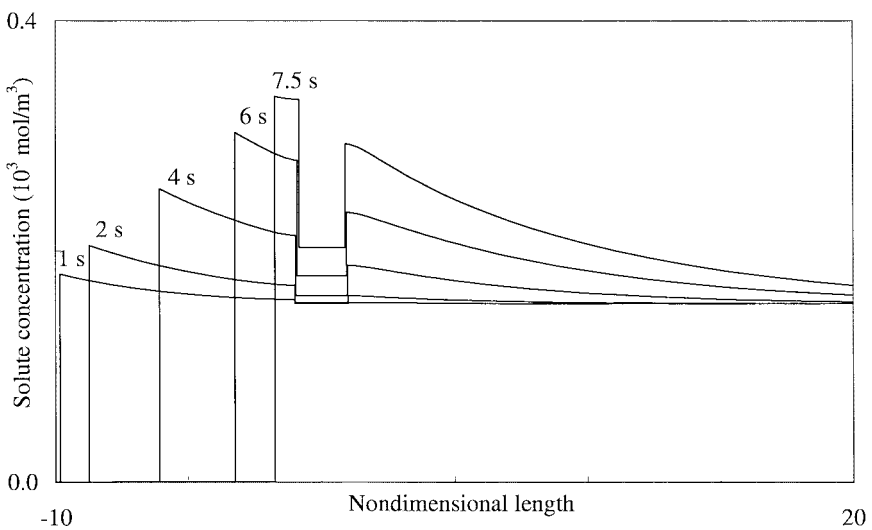

FIG. 20. Salt concentration profiles in a cross section through the middle of the cell (initial front-cell distance of 52.5 μm).

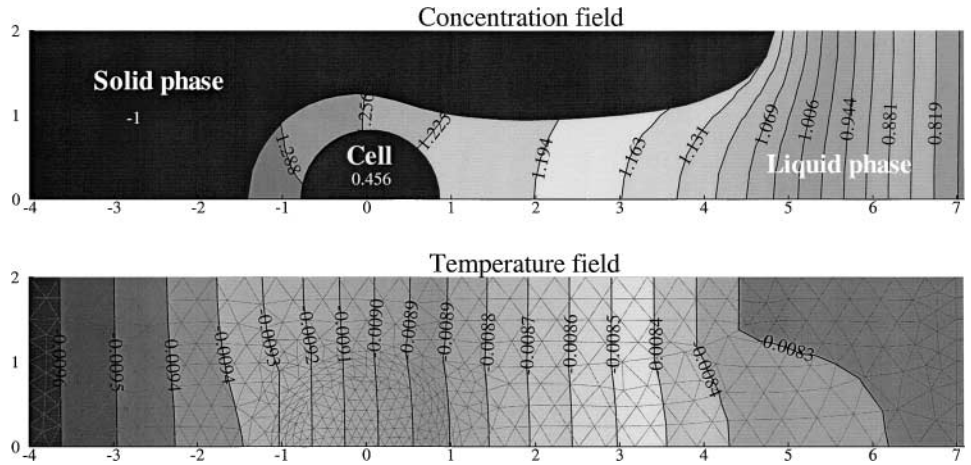

FIG. 21. Nondimensional salt concentration and temperature fields ($t = 8.375$ s, initial front-cell distance of 52.5 μm).

gradient decreases ahead of the cell and increases in the channel behind the cell. Figure 21 shows the nondimensional concentration and temperature fields in the cell region when the cell is being engulfed in the unfrozen solution channel. The intracellular concentration is nearly uniform because of the small size of the cell. Note that the isotherms exhibit a discontinuity corresponding to the location of the solidification front.

In Fig. 22, we compare the osmotic response of the cell for two initial cell locations. The cell shrinkage is delayed when the initial gap between the cell and the liquid–solid interface is increased. This can be explained by the variation with time of the solute concentration. Far from the solidification front, the solute concentration remains nearly constant for a relatively long period before it starts increasing rapidly. Therefore, a cell initially located far from the solidification front undergoes substantial water loss later than a cell initially closer

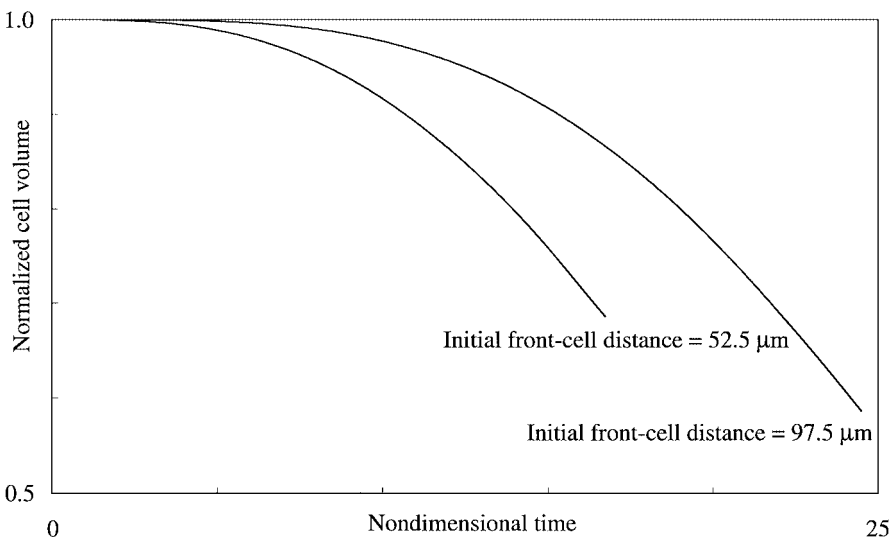

FIG. 22. Normalized cell volume versus nondimensional time.

to the ice front. The influence of the cell position on the osmotic response is generally not taken into account by the analytical models currently used in cryobiology. Indeed, these models are based on the assumption that the temperature and solute concentration distribution are uniform in the cryopreserved cell suspension during the freezing processes. Our numerical results suggest that the cell response is greatly influenced by the location of the cells in the sample, therefore affecting the survival rate of the cells in the cell suspension. The influence of cell location on the cell water loss has been studied by Viskanta *et al.* [44]. In his work, the freezing of a sodium chloride solution without cells was simulated. The calculated temperature and salt concentration profiles were then used to predict the kinetics of water loss from a model cell. However, Viskanta's approach does not take into account how the presence of cells affects the solute concentration and temperature distributions.

The FTALE approach is easy to implement and not excessively time consuming. For example, in the present example, for a total computational time of about 0.3 s per time step on a Sun Sparc Ultra 5 station (330 MHz), less than 26% of the computational time was spent in the subroutines involved in the FTALE treatment. More precisely, 8% of the time was used to compute the geometrical properties of the interface (normal vectors, curvature) by a cubic spline interpolation and 12% to compute the level set field ϕ (signed distance to the nearest interface). Only 3% of the time was used by the domain-mesh fitting process. In future work, the cost of the FTALE approach and methods of reducing it should be considered, especially for the computation of the signed distance to the interface. One approach, as in the level set method, is to limit the computation to the nodes located near the interface.

5. CONCLUSION

In the present paper, we presented the FTALE (front-tracking ALE) method. It is a new approach to solving problems of continuum mechanics with moving interfaces on a fixed grid. Each interface is numerically represented by its own mesh and is moved in a Lagrangian manner typical of a front-tracking approach. The problem of interface singularities, like reconnection, has not been considered although it is not an insurmountable problem for front-tracking methods (see, e.g., [9]). The domain mesh on which the problem of continuum mechanics is solved is continuously fitted to the interface location by moving the nodes nearest to the interface. This temporary local motion of the mesh is taken into account through an unusual ALE formulation. The method does not suffer from the smearing of interface discontinuities common to fixed-grid methods, and by design it can handle interfaces for which the interface jump conditions are critical to evaluating their speed. The model has been developed in the finite element framework for fully unstructured triangular meshes.

Using this FTALE approach, we have developed a two-dimensional model to study the freezing of cell suspensions in a salt solution. The model simulates conduction and diffusion of the solute in the cell region ahead of the growing ice front. The aim is to predict the osmotic response of the cells and their interaction with the ice front, as both are crucial for cell survival during cryopreservation. In contrast to existing models, it is able to handle nonuniform temperature and solute concentration fields. Moreover, the perturbation induced by the cell on the concentration field and its effect on the evolution of the ice front are taken into account. We have reported convergence studies which show that the model

predicts accurately the kinetics of liquid–solid phase change as well as the osmotic motion of cell membranes.

The speed of the solidification front in the phase-change problem is determined via a weak formulation of the Stefan condition, as suggested in [31]. We have demonstrated that oscillations which may arise from a nonuniform triangular discretization can be damped in a heat-conserving way by adding diffusionlike terms to this weak formulation. The addition of this feature for stabilizing Stefan problems allows larger time steps. In the case of unstable crystal growth problems the artificial diffusion must be reduced to accurately predict the instability process. In this case, the smoothing of the interface is accomplished by the stabilizing action of the curvature (Gibbs–Thomson effect). Thus, the savings in computational time is limited, and it could be that a filtering of the perturbation at the element scale would be more efficient.

The potential of the present model to better clarify the damage mechanisms in cell cryopreservation and as an aid in the optimization of cryopreservation protocols has been demonstrated. However, in many situations it will be necessary to consider also convection in the liquid phase, the mechanical action of the membrane, and a cryoprotectant agent in the extracellular medium. These extensions are straightforward within the FTALE framework.

We believe that the general FTALE methodology can also be applied to other problems. For example, the control of incorporation of foreign particles in a host phase during solidification is of prime interest in material processing, but a satisfactory theory for the interaction of a solid particle with a solidification front is still missing. As shown in [45], this problem is tractable with the FTALE model.

ACKNOWLEDGMENTS

Funding for this work was provided by the French Ministere de la Defense through DGA Contract 993404400/DSP. We thank Pr. J. Wolfe for helpful discussions concerning the biophysical part of this work and Dr. J. S. Mullen for comments on the presentation.

REFERENCES

1. J. M. Floryan and H. Rasmussen, Numerical methods for viscous flows with moving boundaries, *Appl. Mech. Rev*. **42**, 323 (1989).
2. W. J. Rider and D. B. Kothe, Reconstructing volume tracking, *J. Comput. Phys*. **141**, 112 (1998).
3. R. Scardovelli and S. Zaleski, Direct numerical simulation of free-surface and interfacial flow, *Annu. Rev. Fluid Mech*. **31**, 567 (1999).
4. S. Osher and J. A. Sethian, Fronts propagating with curvature-dependent speed: Algorithms based on Hamilton–Jacobi formulations, *J. Comput. Phys*. **79**, 12 (1988).
5. J. A. Sethian, *Level Set Methods* (Cambridge Univ. Press, Cambridge, UK, 1996).
6. A. Karma and W. J. Rappel, Quantitative phase-field modeling of dendritic growth in two and three dimesions, *Phys. Rev*. *E* **57**, 4323 (1998).
7. D. Jacqmin, Calculation of two-phase Navier–Stokes flows using phase-field modeling, *J. Comput. Phys.* **155**, 96 (1999).
8. J. Glimm, O. McBryan, R. Menikoff, and D. H. Sharp, Front tracking applied to Rayleigh-Taylor instability, *SIAM J. Sci. Stat. Comput*. **7**(1), 230 (1986).
9. S. O. Unverdi and G. Tryggvason, A front-tracking method for viscous, incompressible, multi-fluid flows, *J. Comput. Phys*. **100**, 25 (1992).

10. G. Tryggvason, *et al., Computations of Multiphase Flows by a Finite Difference/Front-Tracking Method*, Von Karman Institute for Fluid Dynamics Lecture Series 1998-03 (1998).
11. B. T. Helenbrook, L. Martinelli, and C. K. Law, A numerical method for solving incompressible flow problems with a surface of discontinuity, *J. Comput. Phys*. **148**, 366 (1999).
12. R. P. Fedkiw, T. Aslam, B. Merriman, and S. Osher, A non-oscillatory eulerian approach to interfaces in multimaterial flows (the ghost fluid method), *J. Comput. Phys*. **152**, 457 (1999).
13. T. J. Barth and J. A. Sethian, Numerical schemes for the Hamilton–Jacobi and level set equations on triangulated domains, *J. Comput. Phys*. **145**, 1 (1998).
14. A. Brebbia, J. C. F. Telles, and L. C. Wrobel, *Boundary Element Techniques* (Springer-Verlag, Berlin/Heidelberg, 1984).
15. C. Pozrikidis, *Boundary Integral and Singularity Methods for Linearized Viscous Flow* (Cambridge Univ. Press, Cambridge, UK, 1992).
16. C. W. Hirt, A. A. Amsden, and J. L. Cook, An arbitrary Lagrangian–Eulerian computing method for all flow speeds, *J. Comput. Phys*. **135**, 203 (1997), reprinted from *J. Comput. Phys*. **14**, 227 (1974).
17. T. J. R. Hughes, W. K. Liu, and T. K. Zimmermann, Lagrangian–Eulerian finite element formulation for incompressible viscous flows, *Comput. Methods Appl. Mech. Eng*. **29**, 329 (1981).
18. T. Belytschko, D. P. Flanagan, and J. M. Kennedy, Finite element methods with user-controlled meshes for fluid-structure interaction, *Comput. Methods Appl. Mech. Eng*. **33**, 669 (1982).
19. J. Donea, S. Giuliani, and J. P. Halleux, An arbitrary Lagrangian–Eulerian finite element method for transient dynamic fluid-structure interactions, *Comput. Methods Appl. Mech. Eng*. **33**, 689 (1982).
20. D. E. Fyfe, E. S. Oran, and M. J. Fritts, Surface tension and viscosity with lagrangian hydrodynamics on a triangular mesh, *J. Comput. Phys*. **76**, 349 (1988).
21. P. J. Shopov and P. D. Minev, The unsteady motion of a bubble or drop towards a liquid-liquid interface, *J. Fluid Mech*. **235**, 123 (1992).
22. J. Fukai, Z. Zhao, D. Poulikakos, C. M. Megaridis, and O. Miyatake, Modeling of the deformation of a liquid droplet impinging upon a flat surface, *Phys. Fluids* A **5**, 2588 (1993).
23. T. E. Tezduyar, M. Behr, and J. Liou, A new strategy for finite element computations involving moving boundaries and interfaces—the deforming-spatial-domain/space-time procedure: I. The concept and the preliminary numerical tests, *Comput. Methods Appl. Mech. Eng*. **94**, 339 (1992).
24. T. E. Tezduyar, M. Behr, and J. Liou, A new strategy for finite element computations involving moving boundaries and interfaces—the deforming-spatial-domain/space-time procedure: II. Computation of free-surface flows, two-liquid flows, and flows with drifting cylinders, *Comput. Methods Appl. Mech. Eng.* **94**, 353 (1992).
25. P. J. Zwart, G. D. Raithby, and M. J. Raw, The integrated space-time finite volume method and its application to moving boundary problems, *J. Comput. Phys*. **154**, 497 (1999).
26. T. Sato and S. M. Richardson, Numerical simulation method for viscoelastic flows with free surfaces-fringe element generation method, *Int. J. Numer. Methods Fluids* **19**, 555 (1994).
27. F. Mashayek and N. Ashgriz, A hybrid finite-element-volume-of-fluid method for simulating free surface flows and interfaces, *Int. J. Numer. Methods Fluids* **20**, 1363 (1995).
28. N. Lock, M. Jaeger, M. Medale, and R. Occelli, Local mesh adaptation technique for front tracking problems, *Int. J. Numer. Methods Fluids* **28**, 719 (1998).
29. M. Carin, *Etude Microscopique et Macroscopique des Transferts de Chaleur et de Masse dans un Procédé de Congelation de Cellules Vivantes*, Thèse de Doctorat (Université de Provence, 2000).
30. R. P. Batycky, R. Hammerstedt, and D. A. Edwards, Osmotically driven intracellular transport phenomena, *Philos. Trans. R. Soc. London Ser. A* **355**, 2459 (1997).
31. D. R. Lynch and J. M. Sullivan, Jr., Heat conservation in deforming element phase change simulation, *J. Comput. Phys*. **57**, 303 (1985).
32. J. Yoo and B. Rubinsky, A finite element method for the study of solidification processes in the presence of natural convection, *Int. J. Numer. Methods Eng*. **23**, 1785 (1986).
33. D. J. McDaniel and N. Zabaras, A least-squares front-tracking finite element method analysis of phase change with natural convection, *Int. J. Numer. Methods Eng*. **37**, 2755 (1994).

34. Y. Ruan, B. Q. Li, and J. C. Liu, A finite element method for steady-state conduction-advection phase change problems, *Finite Element Anal. Design* **19**, 153 (1995).
35. M. Jaeger, M. Carin, M. Medale, and G. Tryggvason, The osmotic migration of cells in a solute gradient, *Biophys. J*. **77**, 1257 (1999).
36. P. Mazur, Kinetics of water loss from cells at subzero temperatures and the likelihood of intracellular freezing, *J. Gen. Physiol*. **47**, 347 (1963).
37. D. B. Walcerz, Cryosim: A user-friendly program for simulating cryopreservation protocols, *Cryobiology* **32**, 35 (1995).
38. H. S. Carslaw and J. C. Jaeger, *Conduction of Heat in Solids* (Clarendon Press, Oxford, 1959).
39. J. S. Langer, Instabilities and pattern formation in crystal growth, *Rev. Mod. Phys*. **52**, 1 (1980).
40. J. M. Sullivan, Jr., D. R. Lynch, and K. O'Neill, Finite element simulation of planar instabilities during solidification of an undercooled melt, *J. Comput. Phys*. **69**, 81 (1987).
41. J. M. Sullivan, Jr., and D. R. Lynch, Non-linear simulation of dendritic solidification of an undercooled melt, *Int. J. Numer. Methods Eng*. **25**, 415 (1988).
42. K. Wollhöver, C. Körber, M. W. Scheiwe, and U. Hartmann, Unidirectional freezing of binary aqueous solutions: An analysis of transient diffusion of heat and mass, *Int. J. Heat Mass Transfer* **28**, 761 (1985).
43. H. Ishiguro and B. Rubinsky, Mechanical interactions between ice crystals and red blood cells during directional solidification, *Cryobiology* **31**, 483 (1994).
44. R. Viskanta, M. V. A. Bianchi, J. K. Crister, and D. Gao, Solidification processes of solutions, *Cryobiology* **34**, 348 (1997).
45. M. Carin and M. Jaeger, Numerical simulation of the interaction of biological cells with an ice front during freezing, *Eur. Phys. J. AP* **16**, 231 (2001).